PHYSICAL REVIEW A **82**, 013402 (2010)

Unified understanding of tunneling ionization and stabilization of atomic hydrogen in circularly and linearly polarized intense laser fields

Haruhide Miyagi and Kiyohiko Someda

Department of Basic Science, Graduate School of Arts and Sciences, The University of Tokyo, Komaba, Meguro-ku, Tokyo 153-8902, Japan

(Received 26 March 2010; published 6 July 2010)

On the basis of the Floquet formalism, the ionization mechanisms of atomic hydrogen in circularly and linearly polarized intense laser fields are discussed. By using the complex scaling method in the velocity gauge, the pole positions of the scattering-matrix on the complex quasienergy Riemann surface are calculated, and pole trajectories with respect to the variation of the laser intensity are obtained. In the low-frequency regime, the pole trajectory exhibits a smooth ponderomotive energy shift in the case of circular polarization. In contrast, the smoothness is lost in the case of linear polarization. In the high-frequency regime, the pole trajectories exhibit the stabilization phenomenon for both the types of polarization. These observations are elucidated by a unified picture based on the analysis of the adiabatic potentials for the radial motion of the electron in the acceleration gauge. The ionization in the case of circular polarization of the low-frequency regime is governed by the electron tunneling through a barrier of a single adiabatic potential. The stabilization in the high-frequency regime can be explained by the change in the avoided crossings among the adiabatic potential curves. The transition between the different frequency regimes is explicable by the change in the structure of the adiabatic potentials. The difference caused by the type of polarization is ascribable to the difference in the space-time symmetry.

DOI: 10.1103/PhysRevA.82.013402 PACS number(s): 32.80.Rm, 42.50.Hz, 32.80.Fb

I. INTRODUCTION

Intense lasers have been extending the frontiers of atomic physics. Many novel and intriguing phenomena have been found to be caused by nonperturbative atom-laser interactions. In particular, mechanisms of ionization have extensively been studied because ionization is one of the most dominant processes in intense laser fields. Tunneling ionization is known to be typically observed in laser fields of the low-frequency regime [1]. As a phenomenon peculiar to the high-frequency regime, several theoretical studies have predicted the stabilization phenomenon [2–4], in which the ionization rate decreases, in a counterintuitive manner, with increasing laser intensity when intensity exceeds a certain critical value. The low- and high-frequency regimes have independently been studied based on the approximations which are valid only within each regime. In this context, the authors have recently presented a unified picture which explains how different ionization mechanisms work in the different frequency regimes [5]. That previous study is hereafter referred to as Paper I. In Paper I, a two-dimensional (2D) model mimicking an atom having one electron is theoretically analyzed, and it is shown that the transition between the different frequency regimes can be explained by the change in the avoided crossings among the adiabatic potential curves for the radial motion of the electron. The present study aims at demonstrating applicability of the theory of Paper I to the real system, i.e., atomic hydrogen.

The hydrogen atom takes the most fundamental position as the simplest realistic system, in the study of interaction between matter and intense lasers. Many studies have been reported since the work of Keldysh [6], in which the ionization in the tunneling regime was discussed for the first time. As regards the high-frequency regime, Pont *et al.* discussed the energy shift and the distortion of electronic wave functions within the Kramers-Henneberger (KH) high-frequency approximation [7–9]. Pont and Gavrila predicted the stabilization phenomenon by calculating complex quasienergy eigenvalues on the basis of the high-frequency Floquet theory (HFFT) [10]. Behaviors of complex quasienegy eigenvalues have extensively been studied for a wide range of laser intensities and frequencies on the basis of the Floquet complex scaling method [11–13] and the R-matrix Floquet method [14–16]. These rigorous methods have helped the progress in the studies of the stabilization phenomenon [17] and the generation of a light-induced state (LIS) [17,18]. The Floquet method has successfully been applied also to the phenomena typical of the low-freqeuncy regime, such as tunneling ionization [19,20] and high-harmonic generation [21].

The stabilization is one of the typical phenomenon caused by nonperturbative effects of atom-laser interactions. Gavrila named the stabilization phenomenon observed in the Floquet formalism as “quasistationary (adiabatic) stabilization” (QS) [2]. Several researchers have proposed different mechanisms of the stabilization phenomenon independently. According to the conventional understanding, the stabilization occurs when the ponderomotive radius, α, exceeds the spread of the initial unperturbed electronic wave function, a_{at}. At this strength of the laser field, the KH potential comes to have a shape of a double well, and thus the KH eigenfunctions begins to exhibit dichotomy [22,23]. Druten *et al.* experimentally observed the stabilization of a Ne atom in a circular Rydberg state ($5g_4$ state) [24]. Piraux and Potvliege have shown that the experimental results can be reproduced by the calculation based on the Floquet formalism and concluded that it is none other than the QS [25], although the experimental condition $\alpha < a_{\mathrm{at}}$ contradicts with the usual understanding based on the dichotomy. The mechanism of QS for circular Rydberg states should thus be ascribed to a physical picture other than the dichotomy of the wave function. Tikhonova and Popov proposed a different mechanism by considering continuum-continuum transition on the basis of the perturbation theory [26]. The understanding of the mechanism of QS working in realistic atoms has not yet been established.

In the present article, the mechanisms of tunneling ionization and stabilization working in atomic hydrogen are discussed on the basis of the method of the analysis developed in Paper I. A synopsis of the previous study is briefly summarized as follows: An electron is trapped in a 2D potential well interacting with a circularly polarized laser field. The potential function is set to be a Gaussian function. Based on the Floquet formalism, the electron dynamics is described by the multichannel scattering, and the ionization is related with a decay of a resonance state. By numerically solving the close-coupling equations under the Siegert boundary condition, the pole positions of the scattering matrix (S matrix) on the complex quasienergy Riemann surface are calculated. The S-matrix pole trajectories, i.e., the intensity dependence of the pole position, exhibits the behaviors typical of the tunneling ionization in the low-frequency regime and the stabilization in the high-frequency regime. The adiabatic and diabatic potential curves for the radial motion of the electron are found to be useful in elucidating the mechanism of ionization in each frequency regime. In the low-frequency regime, a barrier is formed in the lowest adiabatic curve. The tunneling ionization is interpreted as the electron tunneling through that barrier. It should be noted that the formation of a barrier is not self-evident in the framework of the Floquet formalism which deals with an oscillating field. On the other hand, the stabilization in the high-frequency regime is explicable by the change in the nonadiabatic coupling. With increasing laser intensity, the electron dynamics is more governed by diabatic curves, and the electron is trapped in the diabatic potential well corresponding to the KH potential well.

In the present study, the analysis is carried out on atomic hydrogen (in three dimensional space) interacting with circularly and linearly polarized intense laser fields. The S-matrix pole trajectories are calculated for several laser frequencies covering both the low- and high-frequency regimes. The ionization mechanisms are discussed on the basis of the adiabatic and diabatic potential curves for the radial motion of the electron.

It is found that the picture obtained in Paper I can directly be applied to atomic hydrogen in the high-frequency regime for both the cases of circular and linear polarization. The stabilization is unequivocally explicable by the electron trapping in the KH potential. In the low-frequency regime, however, the type of laser polarization causes a difference in the behaviors of resonance states. The difference is due to the different space-time symmetry. The analysis of the potential curves, however, shows that the picture of tunneling holds valid for both the types of polarization in spite of the significant differences in the structures of the potential curves.

This article is organized as follows. The methods of calculating the S-matrix pole trajectories are described in Sec. II. The space-time symmetry of the resonance states is described in Sec. III. The results of the calculation are shown in Sec. IV. The ionization mechanisms are discussed on the basis of the adiabatic potentials in Sec. V. In Sec. VI, the mechanism of the stabilization is discussed for circular Rydberg states as well as the low-lying states. Section VII concludes this article.

II. FORMULATION

An H atom interacting with circularly or linearly polarized laser fields is considered. The vector potential $\boldsymbol{A}(t)$ is defined in the case of circular polarization as

$$\boldsymbol{A}^{\mathrm{cir}}(t) = -\frac{A}{\sqrt{2}}(\hat{\boldsymbol{x}} \sin \omega t + \hat{\boldsymbol{y}} \cos \omega t), \tag{1}$$

while in the case of linear polarization it is defined as

$$\boldsymbol{A}^{\mathrm{lin}}(t) = -A\hat{\boldsymbol{z}} \sin \omega t. \tag{2}$$

Here, $\hat{\boldsymbol{x}}, \hat{\boldsymbol{y}}$, and $\hat{\boldsymbol{z}}$ are the unit vectors along the x, y, and z axes, respectively. The polarization vector is set perpendicular to the z axis for circular polarization and parallel to the z axis for linear polarization. In the above definitions of the vector potentials, the laser intensity, i.e., the energy flux density of the laser field, are the same for both the polarizations when the magnitudes of A are the same.

A. Complex scaling method in the velocity gauge

The time-dependent Schrödinger equation (TDSE) in the velocity gauge is expressed as

$$i\frac{\partial}{\partial t}\Psi^V(\boldsymbol{r},t) = \left(-\frac{1}{2}\nabla^2 - \frac{1}{r} - i\boldsymbol{A}(t)\cdot\nabla\right)\Psi^V(\boldsymbol{r},t), \tag{3}$$

where $\Psi^V(\boldsymbol{r},t)$ is the wave function in the velocity gauge and $\boldsymbol{A}(t)$ is the vector potential defined in Eqs. (1) and (2). The atomic units are used throughout this article. According to the Floquet theorem, the time-dependent wave function can be written as

$$\Psi^V(\boldsymbol{r},t) = e^{-iEt}\Phi^V(\boldsymbol{r},t), \tag{4}$$

where E is the quasienergy, and the new wave function $\Phi^V(\boldsymbol{r},t)$ has time periodicity with the period $2\pi/\omega$. Substituting Eq. (4) into Eq. (3), one obtains the eigenvalue equation as

$$\begin{aligned} H_{\mathrm{F}}\Phi^V(\boldsymbol{r},t) &\equiv \left(-\frac{1}{2}\nabla^2 - \frac{1}{r} - i\boldsymbol{A}(t)\cdot\nabla - i\frac{\partial}{\partial t}\right)\Phi^V(\boldsymbol{r},t) \\ &= E\Phi^V(\boldsymbol{r},t), \end{aligned} \tag{5}$$

where Floquet Hamiltonian, H_{F}, is defined in the first line.

According to the prescription of Potvliege [12], the wave function $\Phi^V(\boldsymbol{r},t)$ is expanded by the Floquet components, the partial waves in the spherical coordinates (r,θ,ϕ) and the Sturmian basis functions as

$$\Phi^V(\boldsymbol{r},t) = \sum_{Nnlm} c_{Nnlm}\frac{1}{r}S_{nl}^{(\kappa)}(r)Y_{lm}(\theta,\phi)e^{iN\omega t}, \tag{6}$$

where N is the index of the Floquet component, l and m are the angular-momentum quantum number and the magnetic quantum number, respectively, and $S_{nl}^{(\kappa)}(r)$ represents the Sturmian function defined by

$$S_{nl}^{(\kappa)}(r) = \sqrt{\frac{\kappa(n-1)!}{(n+l)(n+2l)!}}(-2\kappa r)^{l+1}e^{-\kappa r}L_{n-1}^{2l+1}(2\kappa r). \tag{7}$$

Here, $L_{n-1}^{2l+1}(\cdot)$ is the associated Laguerre polynomial [27] and κ is a real parameter which scales the coordinate r. By using the expansion in Eq. (6), the eigenvalue equation [Eq. (5)] is reduced to the generalized eigenvalue problem as

$$\boldsymbol{H}_{\mathrm{F}}\boldsymbol{c} = E\boldsymbol{S}\boldsymbol{c}, \tag{8}$$

where $\boldsymbol{S}$ is the overlap matrix due to the nonorthogonality of the Sturmian function. The complex scaling is carried out by scaling the radial coordinate as $r \to e^{i\theta_{\rm r}} r$, where $\theta_{\rm r}$ can vary in the range of $0 \leqslant \theta_{\rm r} < \pi/4$.

B. Close-coupling equations in the acceleration gauge

As discussed in Paper I, the adiabatic and diabatic potential curves in the acceleration gauge are useful in elucidating the ionization mechanisms. In particular, the mechanism of the stabilization in the high-frequency regime can be explained by considering only two channels in the close-coupling equations in the acceleration gauge. The derivation and the explicit form of the close-coupling equations in the acceleration gauge have been reported by several researchers [28,30–32]. However, for the convenience of the discussion in Secs. V and VI, the formulation is briefly summarized as follows.

The TDSE in the acceleration gauge is expressed as

$$i\frac{\partial}{\partial t}\Psi^A(\boldsymbol{r},t) = \left(-\frac{1}{2}\nabla^2 - \frac{1}{|\boldsymbol{r}+\boldsymbol{\alpha}(t)|}\right)\Psi^A(\boldsymbol{r},t), \tag{9}$$

where $\Psi^A(\boldsymbol{r},t)$ is the wave function in the acceleration gauge. The vector $\boldsymbol{\alpha}(t)$ is related to the vector potential $\boldsymbol{A}(t)$ and is defined in the case of circular polarization as

$$\boldsymbol{\alpha}^{\rm cir}(t) = \frac{\alpha}{\sqrt{2}}(\hat{\boldsymbol{x}}\cos\omega t - \hat{\boldsymbol{y}}\sin\omega t), \tag{10}$$

while in the case of linear polarization it is defined as

$$\boldsymbol{\alpha}^{\rm lin}(t) = \alpha\hat{\boldsymbol{z}}\cos\omega t. \tag{11}$$

Here, the ponderomotive radius is defined as $\alpha = A/\omega$ in both the cases of polarization. By the use of the Floquet theorem and the partial wave expansion in the spherical coordinates, the solutions of the TDSE [Eq. (9)] can be expressed as

$$\Psi^A(\boldsymbol{r},t) = e^{-iEt}\sum_{N=-\infty}^{\infty}\sum_{l=0}^{\infty}\sum_{m=-l}^{l}\frac{1}{r}f_N^{lm}(r)Y_{lm}(\theta,\phi)e^{iN\omega t}, \tag{12}$$

where E is the quasienergy. On the other hand, the time-dependent potential function in the TDSE [Eq. (9)] can be expanded in the Fourier series as

$$-\frac{1}{|\boldsymbol{r}+\boldsymbol{\alpha}(t)|} = \begin{cases} \displaystyle\sum_{N=-\infty}^{\infty}\sum_{l=|N|}^{\infty} C_N^l(r;\alpha)Y_{lN}(\theta,\phi)e^{iN\omega t} & \text{(circular polarization)} \\ \displaystyle\sum_{N=-\infty}^{\infty}\sum_{l=0}^{\infty}\tilde{C}_N^l(r;\alpha)Y_{l0}(\theta,\phi)e^{iN\omega t} & \text{(linear polarization),} \end{cases} \tag{13}$$

where definitions of $C_N^l(r;\alpha)$ and $\tilde{C}_N^l(r;\alpha)$ are given in Appendix A (see also Ref. [31] where similar quantities are defined). By substituting Eqs. (12) and (13) into the TDSE [Eq. (9)], one obtains the close-coupling equations in the acceleration gauge. In the case of circular polarization, the explicit form of the close-coupling equations is written as

$$\begin{aligned}&\left(-\frac{1}{2}\frac{d^2}{dr^2} + \frac{l(l+1)}{2r^2} + N\omega\right)g_N^{l\mu}(r) \\ &\quad + \sum_{N'=-\infty}^{\infty}\sum_{l'=|\mu+N'|}^{\infty} V_{NN'}^{ll',\mu}(r;\alpha)g_{N'}^{l'\mu}(r) = Eg_N^{l\mu}(r),\end{aligned} \tag{14}$$

where a new quantum number $\mu = m - N$ is introduced, and a new radial wave function is defined as $g_N^{l\mu}(r) \equiv f_N^{l,\mu+N}(r)$. The interaction potential $V_{NN'}^{ll',\mu}(r;\alpha)$ is given by

$$\begin{aligned}&V_{NN'}^{ll',\mu}(r;\alpha) \\ &\quad = \sum_{l''=s}^{l+l'}(-1)^{N+\mu}C_{N-N'}^{l''}(r;\alpha) \\ &\qquad \times\sqrt{\frac{(2l''+1)(2l'+1)(2l+1)}{4\pi}} \\ &\qquad \times\begin{pmatrix} l'' & l' & l \\ 0 & 0 & 0\end{pmatrix}\begin{pmatrix} l'' & l' & l \\ N-N' & \mu+N' & -\mu-N\end{pmatrix},\end{aligned} \tag{15}$$

where $s = \max\{|N-N'|,|l-l'|\}$ and $(\cdots)$ indicates the Wigner $3j$ symbol. Although the close-coupling equations for circular polarization have been explicitly derived in Refs. [28,31], the quantum number μ was not employed. On the other hand, for linear polarization, the explicit form of the close-coupling equations is expressed as

$$\begin{aligned}&\left(-\frac{1}{2}\frac{d^2}{dr^2} + \frac{l(l+1)}{2r^2} + N\omega\right)f_N^{lm}(r) \\ &\quad + \sum_{N'=-\infty}^{\infty}\sum_{l'=0}^{\infty}\tilde{V}_{N-N'}^{ll',m}(r;\alpha)f_{N'}^{l'm}(r) = Ef_N^{lm}(r),\end{aligned} \tag{16}$$

where the interaction potential $\tilde{V}_{N-N'}^{ll',m}(r;\alpha)$ is expressed as

$$\begin{aligned}&\tilde{V}_{N-N'}^{ll',m}(r;\alpha) \\ &\quad = \sum_{l''=0}^{l+l'}(-1)^m\tilde{C}_{N-N'}^{l''}(r;\alpha)\sqrt{\frac{(2l''+1)(2l'+1)(2l+1)}{4\pi}} \\ &\qquad \times\begin{pmatrix} l'' & l' & l \\ 0 & 0 & 0\end{pmatrix}\begin{pmatrix} l'' & l' & l \\ 0 & m & -m\end{pmatrix}.\end{aligned} \tag{17}$$

In Secs. V and VI, the ionization mechanisms are discussed based on the model in which two selected channels in the acceleration gauge are taken into account. In the analysis of the two-channel model, the S-matrix pole position is calculated on the basis of the R-matrix propagation method as follows: The wave function of the resonance satisfies the Siegert boundary condition

$$g_N^{l\mu}(r),\quad f_N^{lm}(r) \overset{r\to\infty}{\asymp} \text{const.} \times H_l^{(+)}(\eta,k_N r), \tag{18}$$

where $H_l^{(+)}(\eta,k_N r)$ represents the Coulomb function in the form of outgoing spherical wave, $k_N = \pm\sqrt{2(E - N\omega)}$ is the asymptotic momentum of the Nth Floquet channel, and $\eta = -1/k_N$. It should be noted that the Coulomb function is the multivalued function for the complex variable. On the other hand, the boundary condition at the origin is given by the usual form

$$g_N^{l\mu}(r),\quad f_N^{lm}(r) \overset{r\to 0}{\asymp} \text{const.} \times r^{l+1}. \tag{19}$$

The R-matrix propagation is started at a point in a close vicinity of the origin. At a point $r = r_b$ in the asymptotic region, the Siegert boundary condition, Eq. (18), is imposed on the R-matrix $\boldsymbol{R}^{(b)}$. It leads to the secular equation

$$\det\left[\boldsymbol{H}^{(+)}(\boldsymbol{\eta},\boldsymbol{k}r_b) - \boldsymbol{R}^{(b)}\left(\frac{d}{dr}\boldsymbol{H}^{(+)}(\boldsymbol{\eta},\boldsymbol{k}r)\right)_{r=r_b}\right] = 0, \tag{20}$$

from which the complex quasienergy can be determined. The numerical procedures are described briefly in Appendix B.

The R-matrix Floquet method in the velocity gauge has been employed by several researchers [14–16]. Dörr *et al.* mentioned that the same method in the acceleration gauge is numerically unstable [33]. Such a difficulty was not encountered in the calculation of the two-channel model in the present study.

III. SPACE-TIME SYMMETRY PROPERTY

Pont *et al.* discussed the space symmetry property of the KH bound states of atomic hydrogen in circularly and linearly polarized laser fields [7–9]. However, the space-time symmetry property has not sufficiently been studied for the time-periodic system in the framework of the Floquet theory. The TDSE [Eq. (9)] is invariant under the following symmetry operation in the space-time; the space inversion accompanied by the time translation $\delta t = \pi/\omega$, for laser fileds with any polarization. With respect to this generalized parity P defined in the space-time, the eigenstate can be classified into two symmetry species, G (symmetric) and U (antisymmetric). In the case of the linearly polarized laser fields, the TDSE [Eq. (9)] is also invariant under the rotation about the z axis. The magnetic quantum number m thus remains as a good quantum number. It is convenient to employ the symbol $\Lambda = \Sigma,\Pi,\Delta,\ldots$ to specify the value of $|m|$ and classify the manifolds of electronic states as in the spectroscopic notation of diatomic molecules. In the case of circularly polarized laser fields, however, m is not a good quantum number. In this case, the TDSE [Eq. (9)] is invariant under the rotation of angle $\delta\phi$ about the z axis accompanied by the time translation $\delta t = \delta\phi/\omega$. The good quantum number $\mu = m - N$ introduced in Eq. (14) is associated with this symmetry. The manifolds of electronic states can thus be classified by this quantum number as $\mu = 0,\pm1,\pm2,\ldots$. In the KH approximation, i.e., in the limit $\omega \to \infty$, the generalized parity P is reduced to the usual parity with respect to the space inversion, and the system has rotational symmetry about the z axis for both the cases of polarization. The manifolds $\mu = 0$, ±1, $\pm2,\ldots$ are reduced to $\Sigma,\Pi,\Delta,\ldots$, respectively. These definitions are consistent with those used by Pont *et al.* for the classification of the KH bound states [7–9].

The coupling scheme of the close-coupling equations [Eqs. (14) and (16)] within each symmetry manifold is analyzed as follows: In the case of circular polarization, the selection rule of the coupling is given by $|\Delta l| = 1$ and $\Delta m = \Delta N = \pm1$ for the polarization vector lying in the xy plane. For instance, the channel $(l_m,N) = (s,0)$ is coupled with $(p_1,1)$ and $(p_{-1},-1)$. From the latter two channels, chains of coupling further grow involving the channels $(d_2,2),(d_0,0),(d_{-2},-2),\ldots$, and form a tree-diagram in which $(s,0)$ is placed at the apex as shown in Fig. 1(a). This set of channels forms 0_{G} manifold. On the other hand, the set of channels stemming from $(l_m,N) = (s,-1)$ forms 1_{U} manifold. It should be noted that 0_{G} and 1_{U} manifolds have the same physical contents because the both are composed of the same coupling tree, $s \leftrightarrow \{p_1,p_{-1}\} \leftrightarrow \{d_2,d_0,d_{-2}\} \leftrightarrow \ldots$. This is a manifestation of the periodic symmetry of quasienergy spectra in the Floquet formalism. The close-coupling equations [Eq. (14)] are invariant under the replacement $(\mu,N,E) \to (\mu \pm 1,N \mp 1,E \mp \omega)$. Due to the periodicity of the Floquet representation, the replacement $(N,E) \to (N \pm 1,E \pm \omega)$ merely shifts the origin of energy without changing the physical contents of the wave function. Consequently, the replacement $(\mu,N,E) \to (\mu \pm 1,N,E)$ dose not change the physical contents. In other words, the quasienergy spectrum of μ_{G} manifold is the same as that of $(\mu + 1)_{\mathrm{U}}$ with the origin of energy shifted by ω. The periodicity of the quasienergy spectrum is achieved by superposing the sequence of $\{\ldots,(-1)_{\mathrm{U}},0_{\mathrm{G}},1_{\mathrm{U}},\ldots\}$. The independent manifold other than 0_{G} is only 0_{U} which consists of the coupling tree $p_0 \leftrightarrow \{d_1,d_{-1}\} \leftrightarrow \{f_2,f_0,f_{-2}\} \leftrightarrow \cdots$ [see Fig. 1(c)]. In conclusion, it suffices to solve the close-coupling equations only for two manifolds 0_{G} and 0_{U} in the numerical study.

In the case of linear polarization, the selection rule is given by $|\Delta l| = 1$, $\Delta m = 0$ and $|\Delta N| = 1$ for the polarization vector lying parallel to the z axis. The channel $(l_m,N) = (s,0)$ is coupled with $(p_0,1)$ and $(p_0,-1)$. From the latter two channels, a network of coupling further grows as shown Fig. 1(b). Accordingly, the channels satisfying $(l,N) =$ (even,even) or (odd,odd) with fixed m are all coupled to form Λ_{G} manifold. On the other hand, the channels satisfying $(l,N) =$ (even,odd) or (odd,even) forms Λ_{U} manifold. By the Floquet energy shift $(N,E) \to (N \mp 1,E \pm \omega)$, the Λ_{G} manifold is transformed to the Λ_{U} manifold. This indicates that the quasienergy spectrum of Λ_{G} manifold is obtained by simply shifting that of the Λ_{U} manifold by $E \to E \pm \omega$. In conclusion, a sequence of G manifold, $\Sigma_{\mathrm{G}},\Pi_{\mathrm{G}},\Delta_{\mathrm{G}},\ldots$, should be calculated in the numerical study.

IV. *S*-MATRIX POLE TRAJECTORIES

The S-matrix pole trajectories are obtained by gradually changing the value of α with fixed ω. The pole trajectories of the 0_{G}(circular polarization) and Σ_{G}(linear polarization) manifolds are shown in Figs. 2 and 3, respectively, for the cases of $\omega = 0.2,0.3,0.4$, and 0.6. These manifolds contain

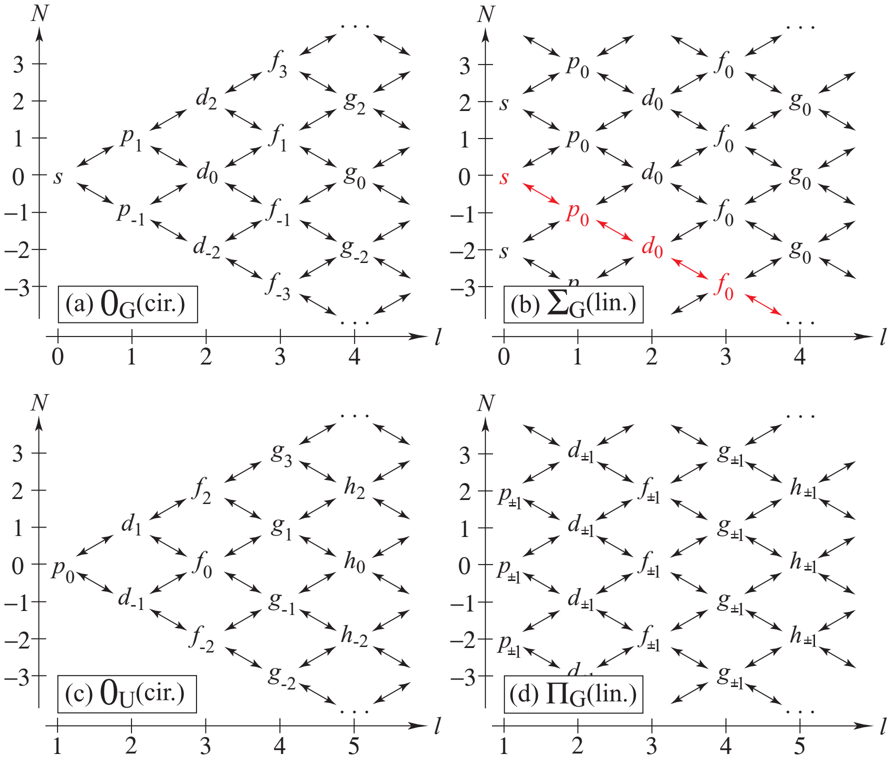

FIG. 1. (Color online) The coupling scheme among the electronic states of atomic hydrogen in circularly and linearly polarized laser fields. The cases of four different symmetry manifolds are shown: (a) 0_G(cir.), (b) Σ_G(lin.), (c) 0_U(cir.), and (d) Π_G(lin.). In each panel, the vertical axis represents the index of the Floquet block, N, and the horizontal axis indicates the angular-momentum quantum number, l. The sequence of (red) symbols in (b) represents the set of channels used to calculate the adiabatic potential curve as discussed in subsection V A2.

the 1s state in the zero field limit. Except for the case of $\omega = 0.6$, the ionization from the 1s state requires multiphoton absorption. The value of $\omega = 0.6$ is used as a representative value for the high-frequency regime, while $\omega = 0.2$ is chosen as that for the low-frequency regime with respect to the 1s state. The others, $\omega = 0.3$ and 0.4, are referred to as the intermediate-frequency regime. Detailed description of the behavior of the observed pole trajectories is given in subsections IV A–IV C.

For the case of circular polarization, the whole quasienergy spectrum can be constructed from the 0_G and 0_U manifolds, as mentioned in Sec. III. The pole trajectories of the 0_U(cir.) manifold is shown in Fig. 4. In the limit of zero field, the lowest state in this manifold is $2p_0$. The one-photon ionization threshold of $2p_0$ corresponds to $\omega = 0.125$. The value of $\omega = 0.2$ is used as a representative value for the high-frequency regime, while $\omega = 0.045$ is chosen as that for the low-frequency regime. In the case of linear polarization, the manifold related with $2p_{\pm 1}$ is the Π_G manifold. The pole trajectories of the Π_G manifold is shown in Fig. 5. The selection of values of ω is the same as 0_U(cir.).

Potvliege and his coworkers have reported numerical studies on the pole trajectories of atomic hydrogen [13]. However, their calculations are restricted to the 0_G(cir.) and Σ_G(lin.) manifolds. Pole trajectories for the 0_U(cir.) and Π_G(lin.) manifolds have not been reported yet. It is emphasized again that the whole quasienergy spectrum for the case of circular polarization can be constructed from the two symmetry manifolds, 0_G(cir.) and 0_U(cir.), both of which are calculated in the present study.

The complex energy plane of mutichannel scattering is composed of Riemannn sheets. It is necessary to specify a Riemann sheet when one describes behaviors of the S-matrix pole trajectories. In the present article, the notation introduced in Paper I is employed. Its definition is briefly summarized below: The asymptotic form of the wave function specifies the Riemann sheet on which the corresponding pole is located. The asymptotic momentum, $k_N = \pm\sqrt{2(E - N\omega)}$, of the Nth Floquet channel, is positive (negative) on the physical (unphysical) sheet with respective to the nth channel. A set of signs of k_n specifies the Riemann sheet uniquely. According to Paper I, the symbol $\Sigma = (\ldots,\sigma_{N-1},\sigma_N,\sigma_{N+1},\ldots)$ is introduced, where σ_N represents the sign of k_N. A pole located in the region $N\omega < \mathrm{Re}E < (N+1)\omega$ is a dominant pole when the combination of sign is given by

$$\begin{aligned}\Sigma &= (\ldots,\sigma_{N-1},\sigma_N,\sigma_{N+1},\sigma_{N+2},\ldots)\\ &= (\ldots,-,-,+,+,\ldots) \equiv \Sigma_N. \end{aligned} \tag{21}$$

Otherwise, the pole is a shadow pole. Here, the symbol Σ_N is defined for the Riemann sheet for the dominant poles in the region $N\omega < \mathrm{Re}E < (N+1)\omega$. The dominant pole is related with the wave function of resonance. On the other hand, shadow pole leads to the wave function with an unphysical boundary condition.

The pole trajectories shown in Figs. 2–5 were calculated by using the complex scaling method (CSM) described in subsection II A. In the expansion of the wave function [Eq. (6)], the Sturmian basis functions up to $n = 40$ were employed. The Floquet channels, $N = -20,\ldots,20$, were taken into account, and 15 angular-momentum states were included in each Floquet channel. The setting of the parameter κ is indicated in each figure caption in the form of $E_{\mathrm{St}} = -\kappa^2/2$.

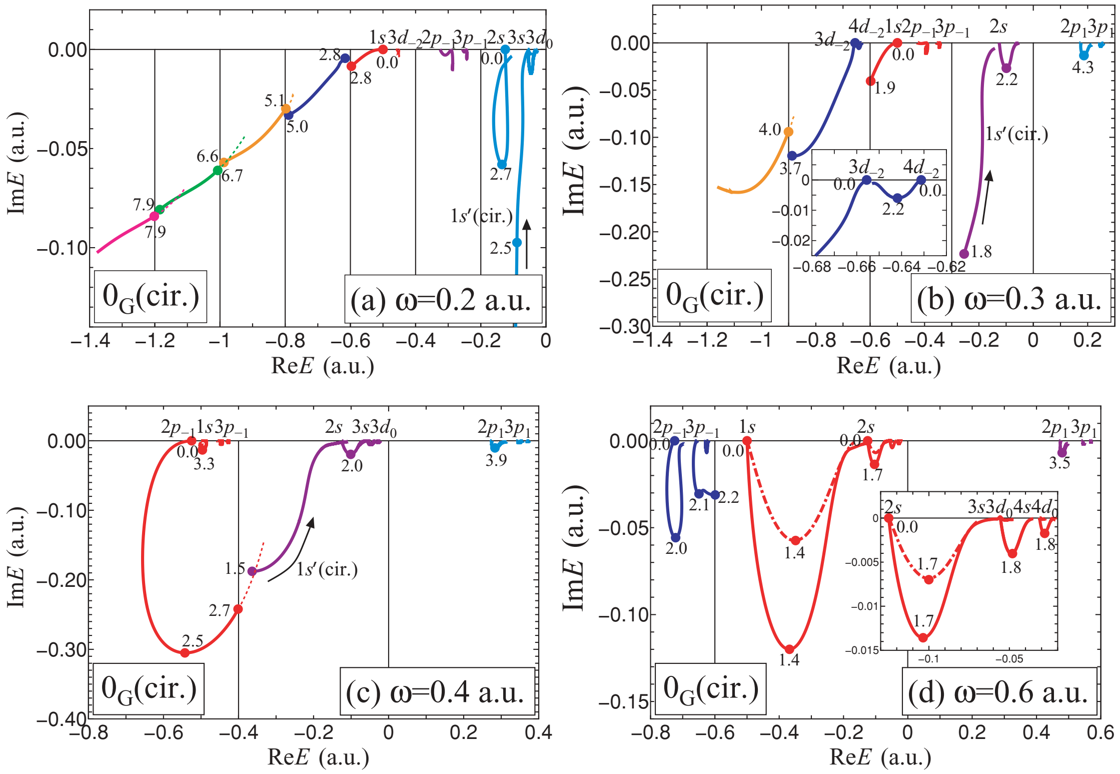

FIG. 2. (Color online) The S-matrix pole trajectories of the 0_G manifold for circular polarization. The cases of four different laser angular frequencies are shown: (a) $\omega = 0.2$, (b) $\omega = 0.3$, (c) $\omega = 0.4$, and (d) $\omega = 0.6$. The pole trajectories are indicated by solid curves when the poles are dominant poles and by dotted curves when they are shadow poles. The vertical lines represent the cuts originating from the branch points at the channel thresholds. The numerical values near the circles indicate the values of α at these points. The symbol, $1s, 2s$, etc., near the real axis represents the state to which the pole correlates in the zero field limit. The insets in (b) and (d) are magnifications of a part of each figure. The dot-dashed (red) trajectories in (d) are the results of the two-channel model, in which the close-coupling equations [Eq. (14)] are solved by including only two channels, $(l_m, N) = (s, 0)$ and $(p_{-1}, -1)$, in the acceleration gauge. The other trajectories were calculated by using the CSM in the velocity gauge with $E_{St} = -0.3$.

A. Low-frequency regime

1. $\mathbf{0_G}$**(cir.)** *manifold*

The pole trajectories of the 0_G manifold for circular polarization in the low-frequency regime ($\omega = 0.2$) are shown in Fig. 2(a). The pole of the $1s$ state becomes the (red) dominant pole on the Σ_{-3} sheet and moves left-downward with increasing laser intensity. That (red) pole crosses the channel threshold Re$E = -0.6$ at $\alpha = 2.8$ and, consequently, becomes a shadow pole. At the same $\alpha = 2.8$, the (blue) pole on the Σ_{-4} sheet crosses the same channel threshold at approximately the same point on the complex energy plane and becomes a dominant pole. It seems that the role of dominant pole is exchanged between these two poles. The (blue) pole on the Σ_{-4} sheet travels left-downward with increasing laser intensity and eventually crosses the channel threshold Re$E = -0.8$. Similarly, the exchange of the role between the (blue) pole on the Σ_{-4} sheet and the (orange) pole on the Σ_{-5} sheet occurs. The sequence of these dominant pole trajectories forms one almost continuous trajectory representing the adiabatic change of the dressed $1s$ state, which is broaden and shifted downward with increasing α. Almost the same behavior has been reported by Shakeshaft *et al.* for circularly polarized laser fields of wavelength $\lambda = 616$ nm ($\omega = 0.074$) [19] and has also been observed in the 2D potential model in Paper I. The line of connected trajectory represents the ponderomotive energy shift, which is known to be typically observed in the tunneling ionization or barrier suppression ionization (BSI).

The behavior of shadow poles is investigated by the R-matrix propagation method in the acceleration gauge (see subsection II B). The (blue) pole on the Σ_{-4} sheet is found to originate from one of the shadow poles of $1s$, while the (orange) pole on the Σ_{-5} sheet originates from one of the shadow poles of $4f_{-3}$. The origins of the (green) pole on the Σ_{-6} sheet and the (pink) pole on the Σ_{-7} sheet have not been assigned. The member poles of the connected trajectory do not necessarily originate from the shadow poles of the $1s$ state.

The dominant pole originating from the $2s$ state on the Σ_{-1} sheet exhibits totally different behavior. The pole moves downward in the interval $0 < \alpha < 2.7$. At $\alpha = 2.7$, the pole turns around and begins to move upward. The upward motion indicates that the ionization rate decreases with increasing laser intensity. This is the stabilization phenomenon. The laser frequency $\omega = 0.2$ corresponds to the high-frequency regime for the $2s$ state, which is bound more weakly than the $1s$ state. Other excited states, $2p_{-1}, 3s, 3p_{-1}, 3d_{-2}$, are also found to exhibit the stabilization phenomenon.

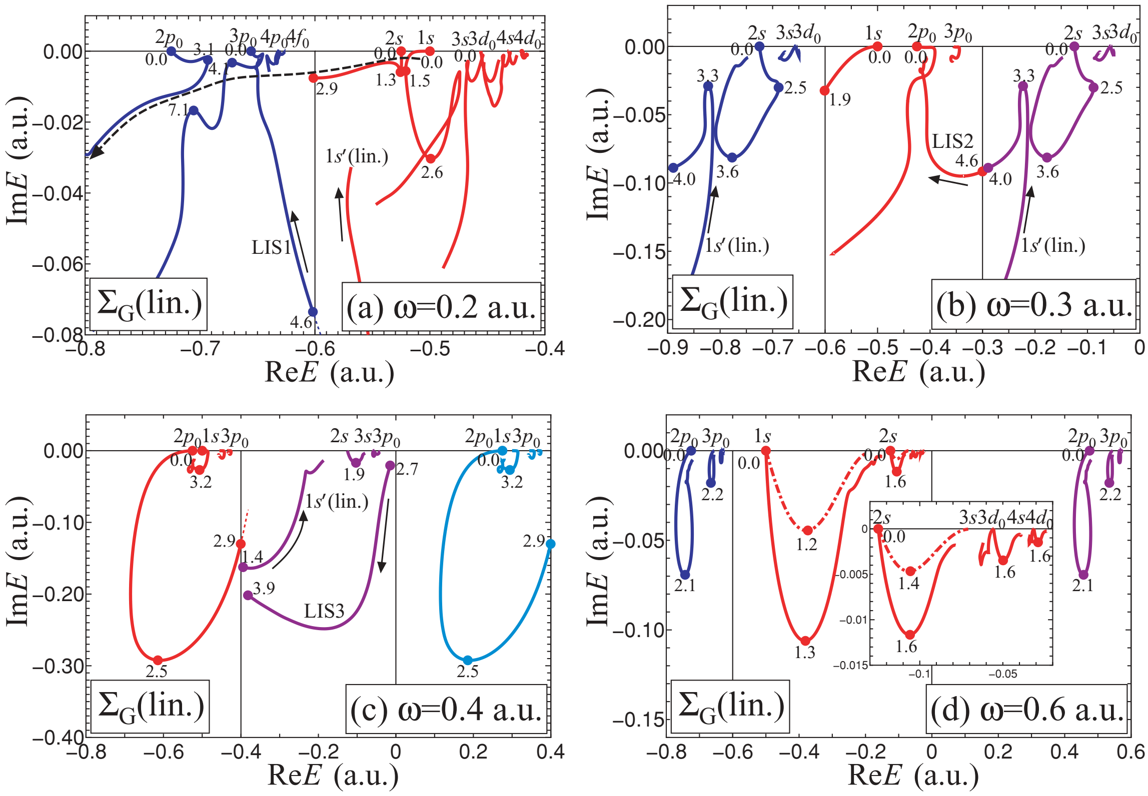

FIG. 3. (Color online) The same as Fig. 2 except that the trajectories in the Σ_G manifold for linear polarization are shown. The dashed line in (a) indicates the ponderomotive energy shift. The dot-dashed (red) trajectories in (d) are the results of the two-channel model including only two channels, $(l_m, N) = (s,0)$ and $(p_0,-1)$, in the acceleration gauge. The other trajectories were calculated by using the CSM in the velocity gauge with $E_{\rm St} = -0.3$.

In Fig. 2(a), one can see a pole which does not originate from the bound state in the zero field limit. It comes from the region $\mathrm{Im}E < -0.20$ and moves upward with increasing laser intensity. This pole corresponds to an LIS and is named $1s'$(cir.) in this article because of the reason which will be discussed in subsection V B. The $1s'$(cir.) state belongs to the LIS of type II in the classification scheme of Potvliege [18]. In this article, LIS's of type II are hereafter indicated by using the symbol of related bound state with a prime. The $1s'$(cir.) state seems to correlate to the $1s'$ state reported by Dörr and Potvliege [17] in the condition of $\omega < 0.5$ for circular and linear polarization.

2. Σ_G(lin.) *manifold*

The pole trajectories of the Σ_G manifold for linear polarization in the low-frequency regime $\omega = 0.2$ are shown in Fig. 3(a). The dominant pole originating from the $1s$ state moves left-downward on the Σ_{-3} sheet and collides with the dominant pole originating from the $2s$ state at $\alpha = 1.3$–1.5. After the collision, the pole of the dressed $1s$ state moves

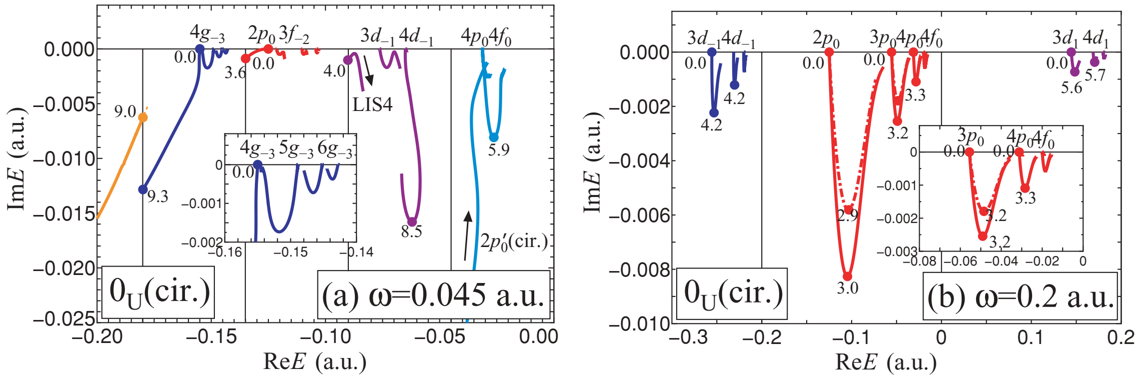

FIG. 4. (Color online) The S-matrix pole trajectories of the 0_U manifold for circular polarization. The cases of two different laser angular frequencies are shown: (a) $\omega = 0.045$ and (b) $\omega = 0.2$. The dot-dashed (red) trajectories in (b) are the results of the two-channel model in the acceleration gauge including only $(l_m, N) = (p_0, 0)$ and $(d_{-1}, -1)$. The other trajectories were calculated by using the CSM in the velocity gauge with $E_{\rm St} = -0.005$ for (a) and -0.05 for (b).

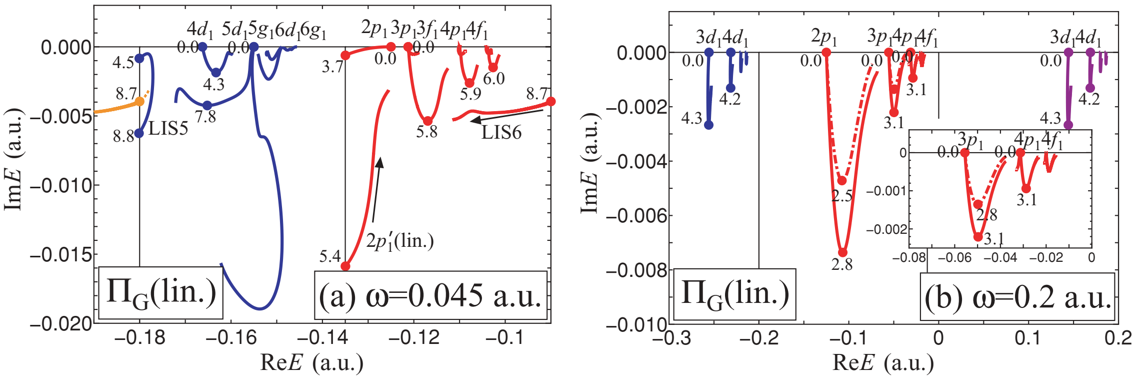

FIG. 5. (Color online) The same as in Fig. 4 except that the trajectories of the Π_G manifold for linear polarization are shown. The dot-dashed (red) trajectories in (b) are the results of the two-channel model in the acceleration gauge including only $(l_m, N) = (p_{\pm 1}, 0)$ and $(d_{\pm 1}, -1)$. The other trajectories were calculated by using the CSM in the velocity gauge with $E_{\mathrm{St}} = -0.005$ for (a) and -0.05 for (b).

right-downward and exhibits the stabilization when $\alpha \geqslant 2.6$, while the pole of the dressed $2s$ state moves leftward and becomes a shadow pole by passing the threshold $\mathrm{Re}E = -0.6$ at $\alpha = 2.9$. The characters of these two poles seem to be exchanged by the collision just like an avoided crossing. If trajectories are traced "diabatically," i.e., the trajectory of the $1s$ pole for $\alpha = 0.0$–1.5 is connected with that of the $2s$ pole for $\alpha = 1.3$–2.9, the resultant trajectory can be regarded as exhibiting the ponderomotive energy shift. Although there is a gap, this ponderomotive energy shift is succeeded by the (blue) dominant poles on the Σ_{-4} sheet: When the precursor (red) dominant pole of the dressed $2s$ state becomes a shadow pole, the (blue) dominant pole of the dressed $4p_0$–$4f_0$ state seems to succeed the line of the ponderomotive energy shift. The $4p_0$–$4f_0$ pole soon collides with the dominant pole of the dressed $3p_0$ state, and the ponderomotive energy shift is succeeded between them by the avoided crossing. A similar succession further occurs from the $3p_0$ pole to the $2p_0$ pole. In contrast to the case of the circular polarization shown in Fig. 2(a), plural number of dominant poles exist on each sheet, and they collide with each other. Despite the interruption at each collision, a line of the ponderomotive energy shift is formed as indicated by the dashed arrow in Fig. 3(a). The energy position, ReE, of each resonance is plotted as a function of α in Fig. 6, where the ponderomotive energy shift can clearly be identified by tracing the curves "diabatically." Similar behavior of pole trajectories was reported by Shakeshaft *et al.* [19]. In summary, the pole trajectories of the Σ_G(lin.) manifold exhibit the ponderomotive energy shift, implying the tunneling ionization or BSI. In contrast to the case of the 0_G(cir.) manifold, however, the avoided crossings caused by collisions among the poles destroy the smooth adiabatic change. These collisions are the essential feature of the case of linear polarization. In the case of circular polarization, the pole trajectory of the dressed $1s$ state runs without any collision due to the existence of the quantum number μ. The case of linear polarization has "lower" symmetry as discussed in Sec. III. The difference in the space-time symmetry causes the dissimilarity between two different cases of polarization.

On the other hand, an LIS appears on the Σ_{-3} sheet by crossing rightward the channel threshold $\mathrm{Re}E = -0.6$. This LIS is named $1s'$(lin.) state. Another LIS (indicated as LIS1) appears on the Σ_{-4} sheet by crossing leftward the threshold $\mathrm{Re}E = -0.6$ at $\alpha = 4.6$.

3. 0_U(cir.) *manifold*

The pole trajectories of the 0_U manifold for circular polarization in the low-frequency regime $\omega = 0.045$ are shown in Fig. 4(a). The (red) dominant pole of the dressed $2p_0$ state moves left-downward and becomes a shadow pole by passing leftward the threshold $\mathrm{Re}E = -0.135$. At this threshold, no dominant pole appears as a successor. On the other hand, the (blue) dominant pole of $4g_{-3}$ on the Σ_{-4} sheet travels left-downward. When this (blue) dominant pole becomes a shadow pole by passing leftward the threshold $\mathrm{Re}E = -0.180$, an (orange) pole appears on the Σ_{-5} sheet. Although the connection is not smooth, a line of the ponderomotive energy shift is formed as in the case of the 0_G(cir.) manifold. On the other hand, there exist two LIS's; a (light blue) pole [indicated as $2p_0'$(cir.)] appears on the Σ_{-1} sheet at large intensity by crossing rightward the threshold $\mathrm{Re}E = -0.045$; and a (purple) pole (indicated as LIS4) appears on the Σ_{-1}

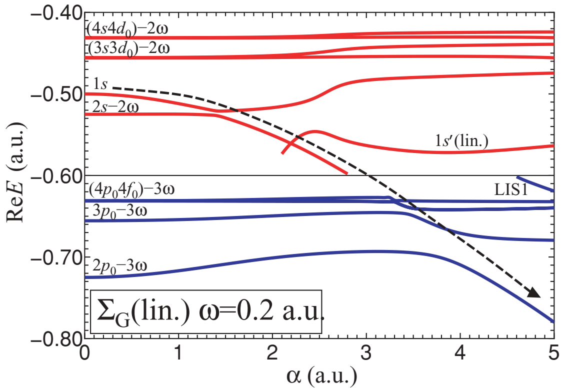

FIG. 6. (Color online) The α dependence of the real parts of quasienergies of the Σ_G manifold for linear polarization in the case of $\omega = 0.2$. The colors of curves correspond to that of the pole trajectories in Fig. 3(a). The dashed line indicates the ponderomotive energy shift.

sheet by crossing rightward the threshold Re$E = -0.090$ at $\alpha = 4.0$.

4. Π_G(lin.) *manifold*

The pole trajectories of the Π_G manifold for linear polarization in the low-frequency regime $\omega = 0.045$ are shown in Fig. 5(a). The pole trajectories can be viewed in a fashion similar to the case of the Σ_G(lin.) manifold. The dominant pole of the dressed $2p_1$ state travels left-downward and becomes a shadow pole by passing leftward the threshold Re$E = -0.135$. No successor appears at this threshold. However, the dominant pole originating from the $5d_1$–$5g_1$ states takes the role of the leftward travel. The leftward motions of these poles can be interpreted as the ponderomotive energy shift. On the other hand, there exist three LIS's; a (red) pole [indicated as $2p_1'$(lin.)] appears on the Σ_{-3} sheet by crossing the threshold Re$E = -0.135$ at $\alpha = 5.4$; a (blue) pole (indicated as LIS5) appears on the Σ_{-4} sheet by crossing the threshold Re$E = -0.180$ at $\alpha = 4.5$; and (red and orange) poles (indicated as LIS6) appear on the Σ_{-3} and Σ_{-5} sheets by crossing leftward each threshold at $\alpha = 8.7$. The LIS5 soon becomes a shadow pole again by recrossing the threshold at $\alpha = 8.8$, but the role of the LIS5 seems to be succeeded by the LIS6.

B. Intermediate-frequency regime

1. 0_G(cir.) *manifold*

The pole trajectories of the 0_G(cir.) manifold in the intermediate-frequency regime ($\omega = 0.3$) are shown in Fig. 2(b). Unlike the case of $\omega = 0.2$, the continuous exchanges of dominant and shadow poles are not seen. The (red) dominant pole of the dressed $1s$ state moves left-downward on the Σ_{-2} sheet and becomes a shadow pole by passing the threshold Re$E = -0.6$. There appears no pole to take the role of the ponderomotive energy shift. On the other hand, the (blue) dominant pole of the dressed $3d_{-2}$ state on the Σ_{-3} sheet travels left-downward and becomes a shadow pole by passing the threshold Re$E = -0.9$. This (blue) pole can be interpreted as a successor of the (red) pole of $1s$ although the connection between them is not continuous. At the threshold Re$E = -0.9$, the role of the (blue) pole in the Σ_{-3} sheet is taken by an (orange) pole on the Σ_{-4} sheet. Therefore, it is only when α is sufficiently large that the ponderomotive energy shift is observed and that the picture of the tunneling ionization holds. This is consistent with the fact that the Keldysh parameter satisfies the tunneling condition ($\gamma < 1$) for $\alpha > 3.33$ in the present case. The other dominant poles on the Σ_{-2}, Σ_{-1}, and Σ_0 sheets exhibit the stabilization. The LIS $1s'$(cir.) appears on the Σ_{-1} sheet as in the case of $\omega = 0.2$. It is emphasized that both the maximum ionization rate of the $2s$ state and the corresponding ponderomotive radius, which is called the critical radius, $\alpha^{\mathrm{cir(c)}}$, in this article, are smaller than those in the case of $\omega = 0.2$. The reason is discussed in subsection VI A based on an intuitive physical picture.

The case of $\omega = 0.4$ are shown in Fig. 2(c). The ponderomotive energy shift is not seen at all. The frequency being set to $\omega = 0.4$; the lowest eigenstate on the Σ_{-2} sheet is $2p_{-1}$ in the limit of zero field. It is the (red) pole of the dressed $2p_{-1}$ state that moves left-downward at first. This can be interpreted as an irregular behavior peculiar to the value of $\omega = 0.4$. Due to the interaction between $1s$ and $2p_{-1}$, their roles are exchanged, and the pole originating from $1s$ exhibits stabilization as $2p_{-1}$ in the case of $\omega = 0.2$ and 0.3. The pole originating from $2p_{-1}$ makes a counterclockwise turn, shows the stabilization, and eventually becomes a shadow pole by passing rightward the threshold Re$E = -0.4$ at $\alpha = 2.7$. Other dominant poles stemming from the original excited states also exhibit stabilization. Both the maximum ionization rate and the critical radius, $\alpha^{\mathrm{cir(c)}}$, of the dressed $2s$ state become smaller than those in the case of $\omega = 0.3$. The LIS $1s'$(cir.) state appears on the Σ_{-1} sheet. This LIS seems to be a successor of the (red) pole of $2p_{-1}$.

2. Σ_G(lin.) *manifold*

The pole trajectories of the Σ_G manifold for linear polarization in the case of $\omega = 0.3$ are shown in Fig. 3(b). On the Σ_{-2} sheet, the (red) dominant pole of the dressed $1s$ state moves left-downward and becomes a shadow pole by crossing the threshold Re$E = -0.6$ at $\alpha = 1.9$. On the other hand, the (blue) dominant pole of the dressed $2s$ state moves right-downward on the Σ_{-3} sheet but changes its direction at $\alpha \simeq 2.5$. The pole seems to take the role of the ponderomotive energy shift. Afterward, the pole of $2s$ exhibits the stabilization when it collides with the (blue) poles [indicated as $1s'$(lin.)] coming upward. The pole of $1s'$(lin.) moves left-downward for $\alpha \geqslant 3.3$ and seems to take the role of the ponderomotive energy shift. The pole of $1s'$(lin.) on the Σ_{-3} sheet crosses the threshold Re$E = -0.9$ at $\alpha = 4.0$. Due to the 2ω periodicity of the quasienergy spectrum of the Σ_G(lin.) manifold, the pole of $1s'$(lin.) can be seem also in the region $-0.3 <$ Re$E < 0$. The pole of $1s'$(lin.) seems to transfer its role to the (red) pole on the Σ_{-2} sheet indicated by LIS2.

The case of $\omega = 0.4$ is shown in Fig. 3(c). On the Σ_{-2} sheet, the (red) pole originating from the $2p_0$ state, which is the lowest eigenstate on this sheet, moves so as to make a counterclockwise turn and eventually becomes a shadow pole by crossing the threshold Re$E = -0.4$ at $\alpha = 2.9$. The LIS $1s'$(lin.) appears on the Σ_{-1} sheet by crossing the threshold Re$E = -0.4$ at $\alpha = 1.4$. The behaviors of these two trajectories resemble those of the dressed $2p_0$ and $1s'$(cir.) in the 0_G(cir.) manifold in Fig. 2(c). Another LIS (indicated as LIS3) appears by crossing leftward the threshold Re$E = 0.0$. This LIS travels leftward and becomes a shadow pole again, by passing leftward the threshold Re$E = -0.4$. The LIS3 shows no stabilization in the limit $\alpha \to \infty$ and can be interpreted as a transient state which does not correlate with the KH bound state.

C. High-frequency regime

The pole trajectories of the 0_G(cir.) and Σ_G(lin.) manifolds for the high-frequency regime $\omega = 0.6$ are shown in Figs. 2(d) and 3(d), respectively. In both the manifolds, the (red) dominant poles of the dressed $1s$ state behaves in almost the same manner: The pole moves right-downward and eventually exhibits the stabilization. It should be noted that the stabilizing part of the dressed 1s trajectory has resemblance to the trajectories of the LIS's $1s'$(cir.) and $1s'$(lin.), which appear in the low- and intermediate-frequency regimes [Figs. 2(a)–2(c) and Figs. 3(a)–3(c)]. The dominant poles originating from the excited ns ($n = 2,3,\ldots$) states on the Σ_{-1} sheet also exhibit the stabilization in the same manner as $1s$ for either cases of polarization. The stabilization of excited states takes place in the range of $\alpha = 1.4$–1.8.

The pole trajectories of the 0_{U}(cir.) and Π_{G}(lin.) manifolds for the high-frequency regime $\omega = 0.2$ are shown in Figs. 4(b) and 5(b), respectively. The pole trajectories of these two manifolds resemble each other and also look similar to those of the 0_{G}(cir.) and Σ_{G}(lin.) manifolds. All the dominant poles move in a similar way and show stabilization at $\alpha = 2.8$–3.3. The insensitivity of the phenomena to the type of polarization can be regarded as common to all the manifolds in the high-frequency regime.

V. ANALYSIS OF THE IONIZATION MECHANISM ON THE BASIS OF THE POTENTIAL CURVES

As discussed in the preceding section, the pole trajectories in the low-frequency regime can be interpreted as exhibiting the ponderomotive energy shift. In the case of circular polarization, particularly, the dominant pole trajectories are almost continuously connected to form the line of the ponderomotive energy shift. Such a smooth ponderomotive energy shift implies that the mechanism of tunneling ionization or BSI is working. In the case of linear polarization, however, the connection between trajectories is less smooth. The line of the ponderomotive energy shift is apt to broken by the collision among the pole trajectories. The validity range of the tunneling mechanism thus seems to depend on the type of laser polarization. On the other hand, the behavior of pole trajectories in the high-frequency regime is found to be dominated by the stabilization for both the types of polarization. In order to explain these observations and to clarify the mechanisms of tunneling ionization and stabilization, the attention is focused on the potential matrix in the close-coupling equations in the acceleration gauge [Eqs. (14) and (16)]. The effective potential matrix is here defined as the interaction potential added by the centrifugal potential. Its explicit form is given by

$$(\boldsymbol{V}^{\mathrm{cir}}_{\mu_P}(r;\alpha))_{NlN'l'} = \left[\frac{l(l+1)}{2r^2} + N\omega\right]\delta_{NN'}\delta_{ll'} + V^{ll',\mu_P}_{NN'}(r;\alpha), \tag{22}$$

for circular polarization and

$$(\boldsymbol{V}^{\mathrm{lin}}_{\Lambda_P}(r;\alpha))_{NlN'l'} = \left[\frac{l(l+1)}{2r^2} + N\omega\right]\delta_{NN'}\delta_{ll'} + \tilde{V}^{ll',\Lambda_P}_{N-N'}(r;\alpha) \tag{23}$$

for linear polarization. The adiabatic potential curves for the radial motion of the electron are obtained by the eigenvalues of the effective potential matrix plotted as a function of r, while the diabatic potential curves can be directly obtained by plotting the diagonal elements. The KH potential curves can be obtained by diagonalizing the block of $N = N' = 0$, $(\boldsymbol{V}^{\mathrm{cir}}_{\mu_P}(r;\alpha))_{N=N'=0}$ or $(\boldsymbol{V}^{\mathrm{lin}}_{\Lambda_P}(r;\alpha))_{N=N'=0}$. The diabatic potential curves in each Floquet block do not cross each other. Consequently, The KH potential curves exhibit no avoided crossing and thus resemble the diabatic potential curve of $N = 0$ block.

In the following subsections, the adiabatic and KH potential curves were calculated by using relatively small number of channels to make the potential diagram more sparse and clear. The Floquet channels taken into account were as follows: $N = -15,\ldots,5$ in the low-frequency regime (subsection V A), and $N = -5,\ldots,5$ in the high-frequency regime (subsection V B). For both the frequency regimes, five angular-momentum states were included in each Floquet block.

A. Low-frequency regime

1. Case of circular polarization

Figure 7 shows the adiabatic, diabatic, and KH potential curves of the 0_{G}(cir.) manifold in the low-frequency regime $\omega = 0.2$. When $\alpha = 0$, the adiabatic, diabatic, and KH potential curves coincide with each other by definition. When α increases, the adiabatic potential curves begin to exhibit avoided crossings with each other. When $\alpha = 2.0$, the lowest adiabatic curve comes to have a barrier, through which the tunneling ionization can take place. At the same time, the effects of the avoided crossings create a new cuspidal potential well separated from the bunch of repulsive potential curves due to the following reason. The lowest diabatic potential, $(\boldsymbol{V}^{\mathrm{cir}}_{0_{\mathrm{G}}}(r;\alpha))_{00,00}$, is a constant in the inner region $0 \leqslant r \leqslant \alpha/\sqrt{2}$ [see Eqs. (15) and (A1)], and its derivative is discontinuous at the boundary point $r = \alpha/\sqrt{2}$. The interaction among channels becomes maximum at the boundary point $r = \alpha/\sqrt{2}$ and decreases exponentially with either increasing and decreasing r. Due to the repulsion among the diabatic curves, the lowest adiabatic curve forms a cuspidal well at the boundary point $r = \alpha/\sqrt{2}$. The original $1s$ state becomes a resonance state held on this potential well when the laser field is switched on. As α increases, the maximum of the interaction shifts toward larger r, and the cuspidal well also shifts along the envelop of the repulsive curves. As a result, the ponderomotive energy shift takes place. When $0 < \alpha < 4$, the resonance state locates inside the potential well. The electron bounded in the cuspidal well tunnels through the potential barrier. When $\alpha \geqslant 4$, the energy of the resonance state exceeds the top of the barrier, and the BSI takes place.

In order to verify this intuitive picture, the calculation of the single-channel scattering for the lowest adiabatic potential is carried out by using the complex absorbing potential (CAP) method. The detail of the calculation is described in Appendix C. The resultant complex energy eigenvalues are shown in Fig. 8 together with the lowest adiabatic potential curves used for the CAP calculation. Slight difference between the lowest adiabatic potential curves in Figs. 7 and 8 is due to the difference in the number of channels considered in the calculation. The adiabatic curves in Fig. 7 are generated by less number of channels in order to make the graph more sparse and clear. It should be noted that the complex energy eigenvalues shown in Fig. 7 were not calculated by using the potential curves shown together but obtained by the accurate calculation based on the CSM. The complex energy eigenvalues shown in Fig. 8 agree with exact ones in Fig. 7. The tunneling ionization and the BSI can be interpreted as decay of the shape resonance formed on the lowest adiabatic potential as in the case of 2D Gaussian potential model (see subsection IVA of Paper I).

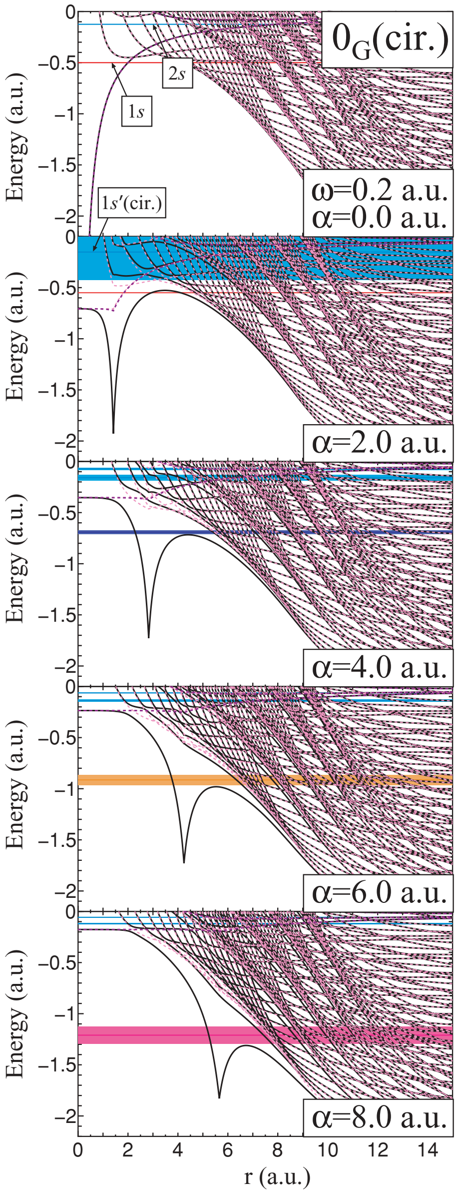

FIG. 7. (Color online) Potential curves for the radial motion of electron of the 0_{G} manifold for circular polarization in the case of the low-frequency regime $\omega = 0.2$. (Black solid curves) Adiabatic potential, (pink dashed curves) diabatic potential, and (purple dashed curves) KH potential. The values of the ponderomotive radius α are shown in each figure. The horizontal bands indicate the positions and widths of several selected resonances corresponding to the dominant poles of the same color in Fig. 2(a).

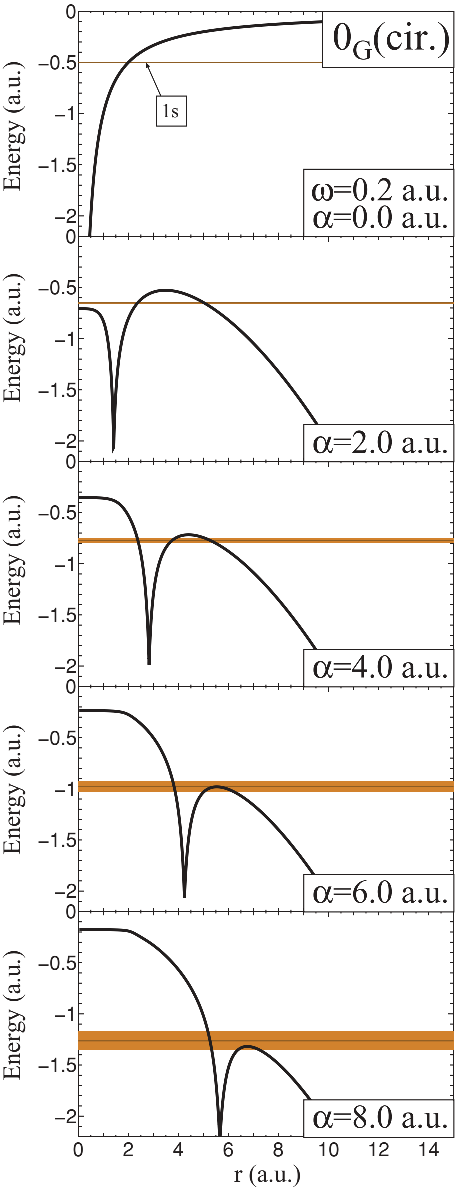

FIG. 8. (Color online) The position and width of the resonance formed in the single-channel scattering on the lowest adiabatic potential of the 0_{G} manifold for circular polarization in the case of the low-frequency regime $\omega = 0.2$. The black solid curve is the lowest adiabatic potential obtained from the calculation. The (brown) horizontal bands indicate the positions and widths of the resonances. In the case of $\alpha = 0.0$, the horizontal line indicates the position of the $1s$ state. The detail of the calculation is described in Appendix C.

On the other hand, the behaviors of the dressed $2s$ state and the LIS $1s'$(cir.) are explicable by the KH potential. As α increases, these states seem to become a resonance state formed on the KH potential. The behavior of this kind is the so-called KH stabilization typical to the high-frequency regime [4]. Its mechanism will be discussed in subsection V B.

The potential curves of the 0_{U}(cir.) manifold is shown in Fig. 9. The ionization mechanism can be explained in a way quite similarly to the case of the 0_{G}(cir.) manifold. When the laser field is switched on, the potential for the np_0 state is deformed to the lowest adiabatic curve with a barrier due to avoided crossings with the other curves. As α increases, the potential well becomes shallower, and the barrier becomes lower. Such a change of the lowest adiabatic curve indicates the ponderomotive energy shift of the dressed $2p_0$ state. The ionization mechanism of the $2p_0$ state is quite similar to that of $1s$ of the 0_{G}(cir.) manifold: Tunneling ionization for $0 < \alpha \leqslant 3$ and BSI for $\alpha > 3$.

In summary, the adiabatic potential curves generated from the effective potential matrix clearly show that the ionization mechanism is explicable by the tunneling of electrons. The ponderomotive energy shift is explained by the change in the

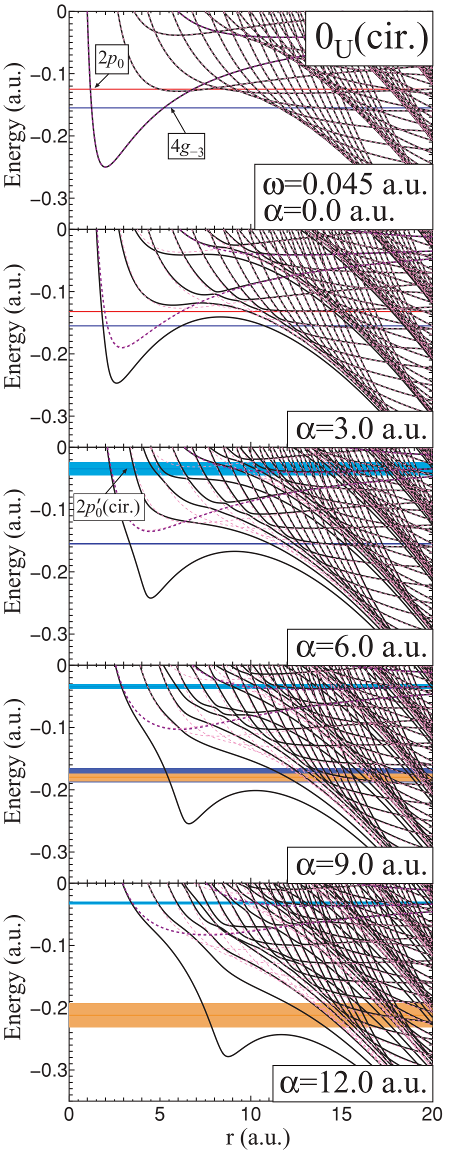

FIG. 9. (Color online) The potential curves of the 0_U manifold for circular polarization in the low-frequency regime ($\omega = 0.045$). The horizontal bands correspond to several selected dominant poles of the same color in Fig. 4(a). See the caption of Fig. 7 for the legend about the curves.

lowest adiabatic curve with increasing laser intensity. It is noteworthy that the electron motion in the ionization process can be understood by the single-channel potential problem. In this respect, there is complete parallelism with the 2D Gaussian potential model in Paper I.

2. *Case of linear polarization*

The potential curves of the Σ_G(lin.) manifold is shown in Fig. 10. The structure of the potential curves differs totally from the case of circular polarization due to the difference in the space-time symmetry property as discussed in Sec. III. In the case of Σ_G(lin.) manifold, the Floquet block of even N contains all the diabatic channels of even l and that of odd N contains all those of odd l. The potential diagram thus becomes 2ω periodic with respect to the quasienergy. In consequence, all the adiabatic curves have to experience many avoided crossings. However, some of the avoided crossings exhibit very small energy gaps. In the case of $\alpha = 1.0$, potential barriers can be seen in every other Floquet interval as indicated in Fig. 10. The existence of such a barrier supports the picture of tunneling ionization. As α increases, the barriers are pushed down, the ponderomotive energy shift being suggested. As α increases further, however, the barriers are destroyed by avoided crossings with large energy gaps. Up to $\alpha = 3.0$, the barriers can be recognized in the potential diagram. In accordance with it, the ponderomotive energy shift of the pole trajectory can almost continuously be traced in Figs. 3(a) and 6 up to $\alpha = 2.9$. In the case of $\alpha = 4.0$, the potential barrier is completely destroyed. In this respect, the situation differs from the case of circular polarization.

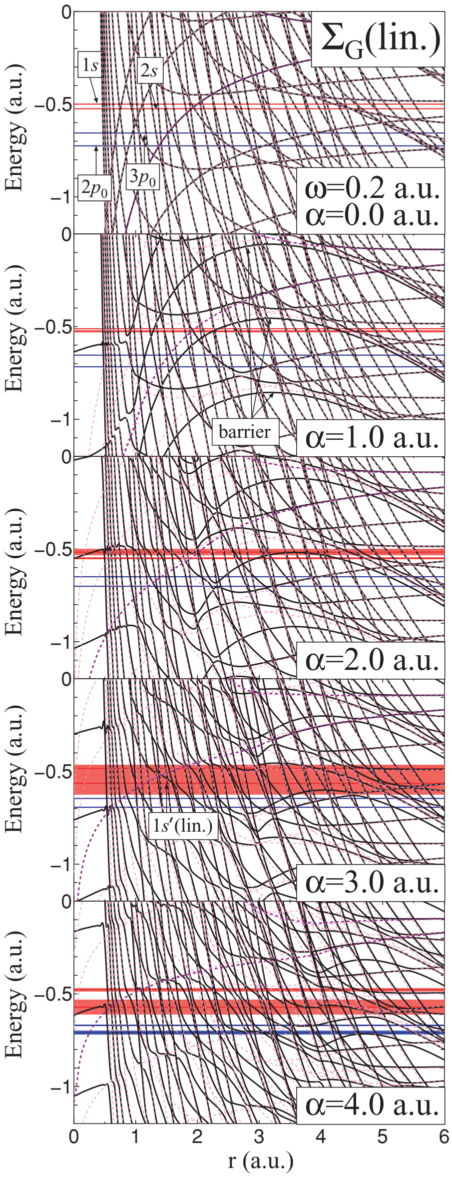

FIG. 10. (Color online) The same as Fig. 7 except that the potential curves of the Σ_G manifold for linear polarization are shown.

In order to verify the tunneling picture, the calculation of the single-channel scattering is carried out. In this case, a

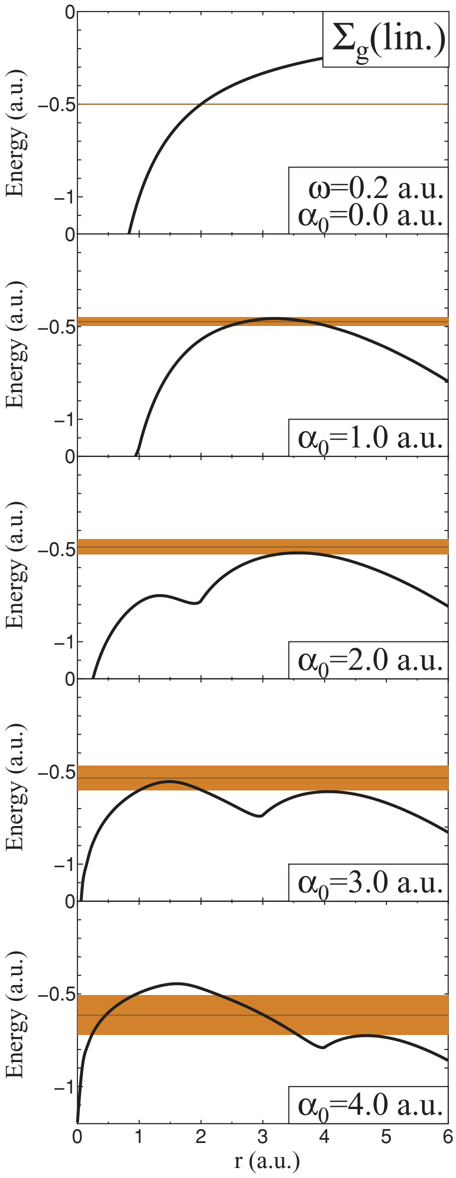

FIG. 11. (Color online) The model potential for the Σ_G(lin.) manifold in the case of the low-frequency regime $\omega = 0.2$. The black solid curve is the lowest adiabatic potential constructed by the selected channels $(s,0),(p_0,-1),(d_0,-2),\ldots$. The (brown) horizontal bands indicate the positions and widths of the resonances formed on the potential curves. In the case of $\alpha = 0.0$, the horizontal line indicates the position of the $1s$ state. The detail of the calculation is indicated in Appendix C.

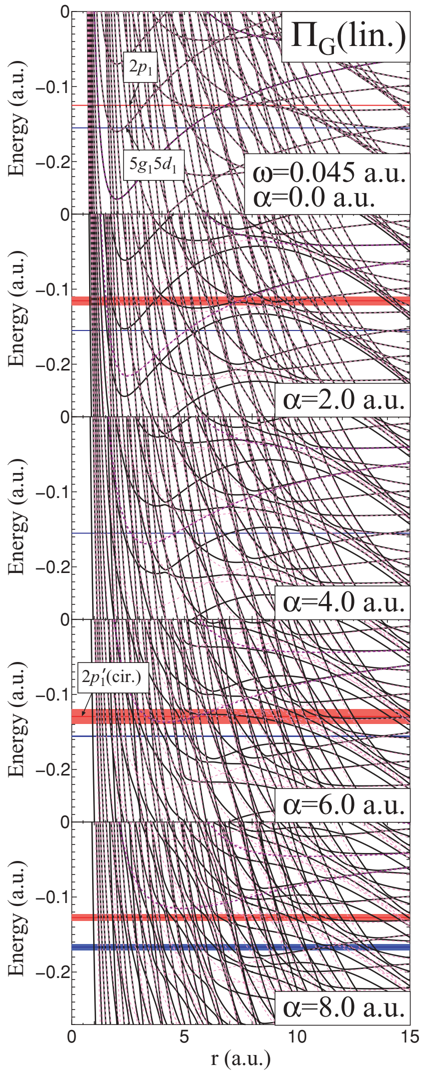

FIG. 12. (Color online) The same as in Fig. 9 except that these are potential curves of the Π_G manifold for linear polarization.

certain modeling is required in order to define a potential curve which will dominate the tunneling. The potential barrier seen in Fig. 10 is constructed by a choice of channels as follows: The channel $(l_m,N) = (s,0)$ is coupled with $(p_0,-1)$ and $(p_0,1)$ [see Fig. 1(b)]. The pair of $(s,0)$ and $(p_0,-1)$ makes a curve crossing, while that of $(s,0)$ and $(p_0,1)$ does not. The channel $(p_0,-1)$ is coupled with $(s,0),(d_0,0),(s,-2)$, and $(d_0,-2)$. Among them only $(s,0)$ and $(d_0,-2)$ make curve crossing with $(p_0,-1)$. A selection based on the curve crossing defines a sequence of channels, $(s,0),(p_0,-1),(d_0,-2),\ldots$, as indicated by (red) symbols in Fig. 1(b). The effective potential matrix constructed by this sequence of channels leads to an adiabatic potential curve as shown in Fig. 11. It roughly reproduces the potential barrier seen in Fig. 10. The complex energy eigenvalue of the resonance formed on the potential curve is calculated and indicated in Fig. 11. The detail of the calculation is described in Appendix C. The complex energy eigenvalues in Fig. 11 do not reproduce the line of ponderomotive energy shift shown in Fig. 3(a). In spite of the existence of the barrier, the decay of the resonance cannot be understood as a single-channel problem due to large avoided crossings in the inner region $r < \alpha$.

The potential curves of the Π_G(lin.) manifold are shown in Fig. 12. The potential barriers are more clearly seen. The avoided crossings in the inner region are smaller than the case of the Σ_G(lin.) manifold. The barriers are pushed down with increasing α and, eventually, destroyed by avoided crossings. For $\alpha < 4.0$, the potential with a well and a barrier can be recognized. In accordance with it, the corresponding pole trajectory in Fig. 5(a) exhibits a smooth ponderomotive energy shift up to $\alpha = 3.7$.

In conclusion, the tunneling mechanism accompanied with the ponderomotive energy shift can be recognized in the case

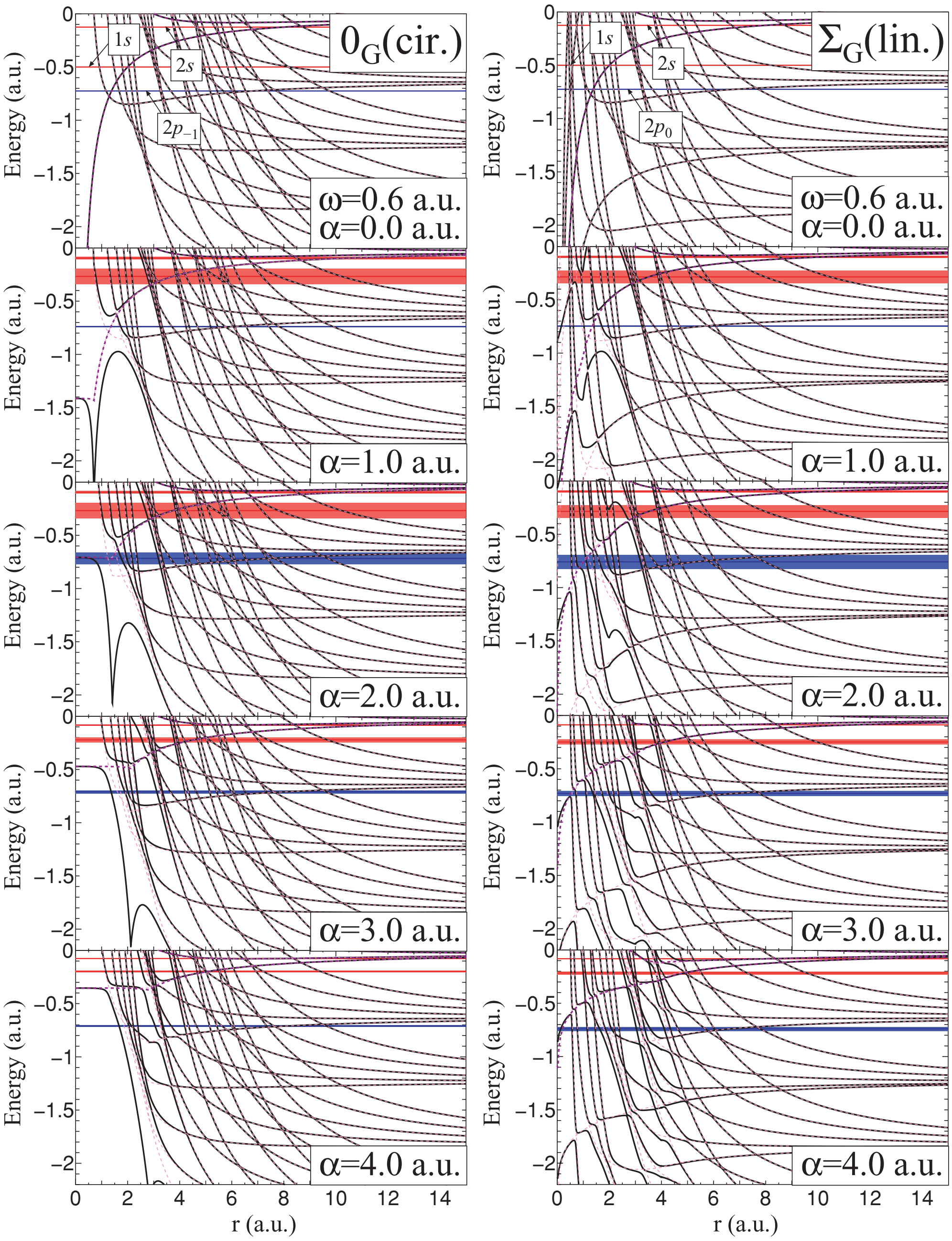

FIG. 13. (Color online) The left and right columns show the potential curves of the 0_G(cir.) and Σ_G(lin.) manifolds, respectively, in the case of high-frequency regime $\omega = 0.6$. See the caption of Fig. 7 for the legend about the curves.

of the linear polarization. However, the decay of the resonance state cannot simply be understood on the basis of the single-channel potential problem due to the avoided crossings in the inner region. The tunneling picture itself becomes inadequate with increasing laser intensity. This situation contrasts with the case of circular polarization, in which the tunneling ionization can be explicable by the single-channel problem of the lowest adiabatic potential. The dissimilarity is ascribable to the difference in the space-time symmetry.

B. High-frequency regime

The potential curves of the 0_G(cir.) manifold in the high-frequency regime $\omega = 0.6$ are shown in the left column of Fig. 13. When $\alpha = 1.0$, the cuspidal potential well is shallower than the case of $\omega = 0.2$ shown in Fig. 7. In the high-frequency regime, the larger channel interval makes the envelope of the diabatic curves steeper, and this situation makes the cuspidal well shallower. For $\alpha \geqslant 1$, therefore, no resonance state is formed on the cuspidal well. In the present case, the dressed 1*s* state shifts upward with increasing α and becomes a resonance state trapped in the well of the potential curve in which the avoided crossing with small gaps are connected diabatically. The resonance state decays due to the avoided crossings. When $\alpha = 1.0$–2.0, the diabatic trapping potential experiences the avoided crossings with large energy gaps, and, consequently, the resonance has a large width. When $\alpha \geqslant 3$, however, the energy gaps decrease, and the stabilization of resonance state

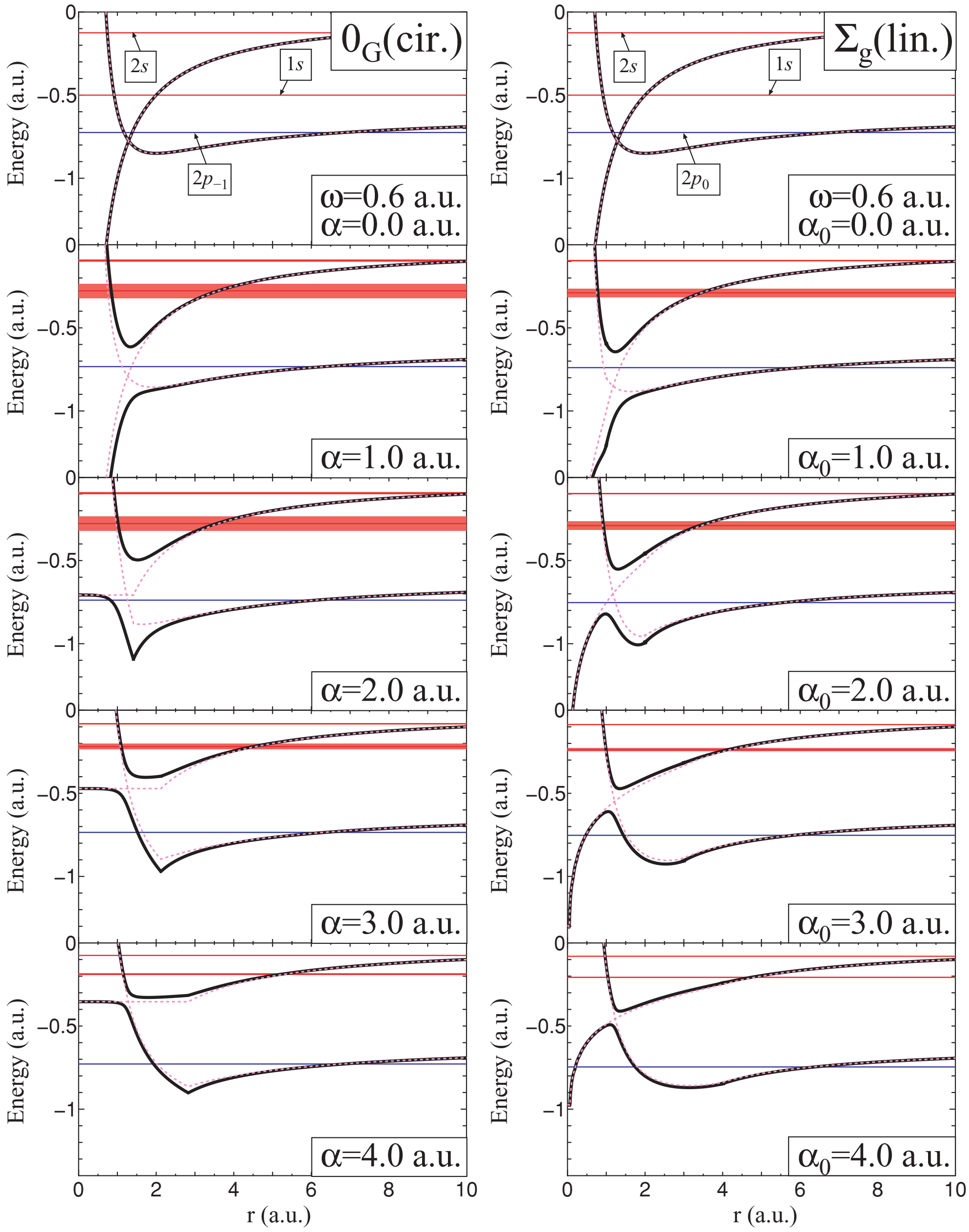

FIG. 14. (Color online) The results of the two-channel model. The left column is the case of circular polarization calculated by considering the two channels, $(l_m, N) = (s,0)$ and $(p_{-1}, -1)$. On the other hand, the right column is the case of linear polarization calculated by considering $(s,0)$ and $(p_0, -1)$. The meaning of the black solid and pink dashed curves are the same as Fig. 7.

takes place. The trapping potential coincides with the KH potential. This is none other than the KH stabilization. The reduction of the energy gap originates from a discrepancy between the crossing point and the maximum of the coupling matrix element as a function of r. This is the same scenario as in the case of 2D model discussed in Paper I. An analysis on the α dependence of the energy gap will be presented in subsection VI A.

The potential curves of the Σ_G(lin.) manifold shown in the right column of Fig. 13 have the structure similar to the 0_G(cir.) manifold except that the cuspidal potential well is not seen. The dressed 1s state shifts upward and becomes a resonance state trapped in the well of the potential curve traced diabatically. When $\alpha = 1.0$–2.0, the trapping potential is destroyed by the avoided crossings with large energy gaps. When $\alpha \geqslant 3.0$, the KH potential is recovered by decreasing energy gaps, and the stabilization occurs. The scenario of the KH stabilization is thus common to both the circular and linear polarizations. The stabilization of the resonance originating from the ns $(n = 0,1,2,\ldots)$ state can qualitatively be explained, for either the case of the 0_G(cir.) and Σ_G(lin.) manifolds, by the two-channel model in which only two channels are taken into account; $(l_m, N) = (s,0)$ and $(p_{-1}, -1)$ for 0_G(cir.); $(l_m, N) = (s,0)$ and $(p_0, -1)$ for Σ_G(lin.). The resonance positions and widths obtained by the two-channel model are shown in Fig. 14 together with the potential curves.

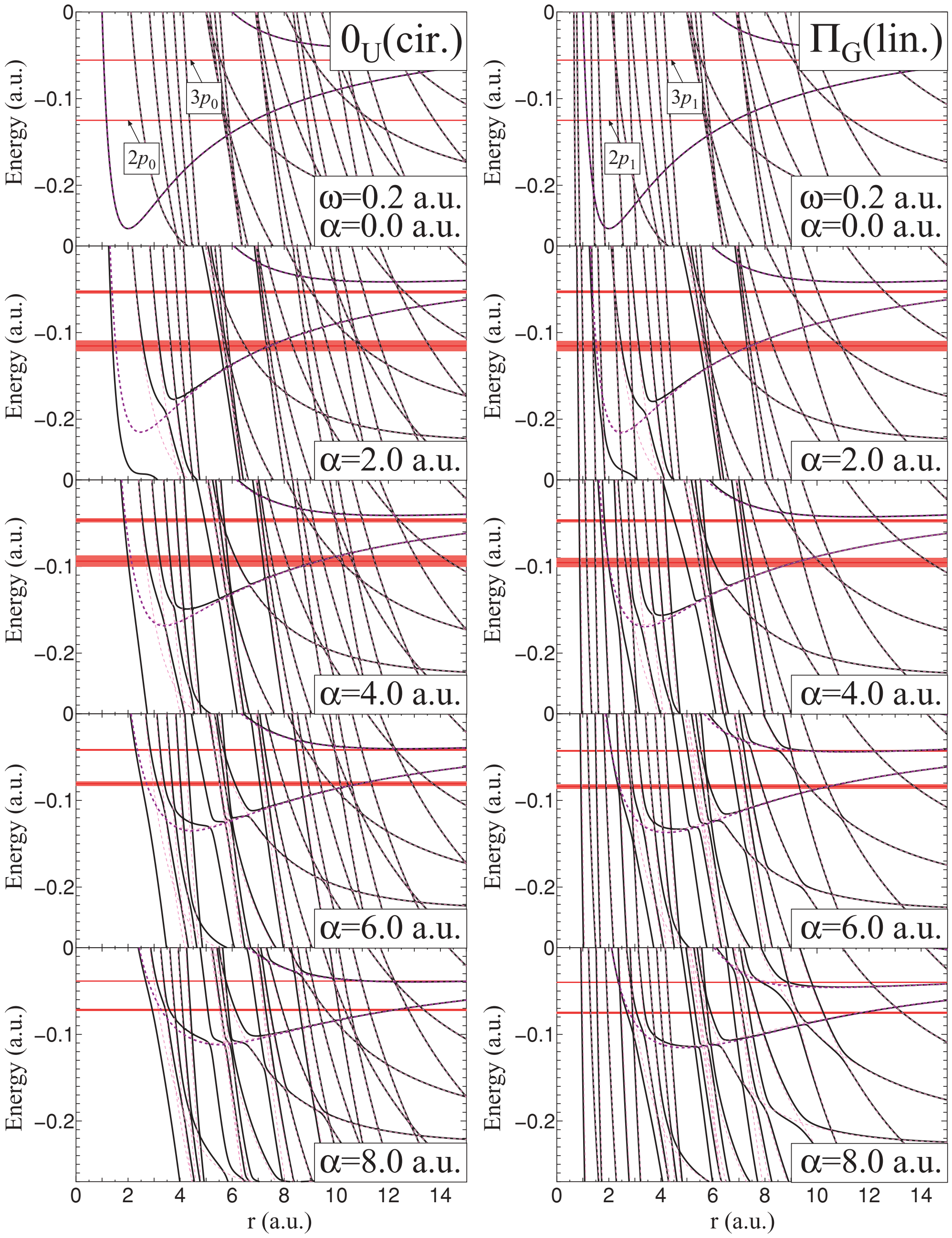

FIG. 15. (Color online) The left and right columns show the potential curves of the 0_{U}(cir.) and Π_{G}(lin.) manifolds, respectively, in the case of high-frequency regime $\omega = 0.2$. See the caption of Fig. 7 for the legend about the curves.

The same data are also shown in the form of pole trajectory in Figs. 2(d) and 3(d). The resonance can be interpreted as the Feshbach resonance, in which the scattering wave in the open channel $(p_{-1},-1)$ or $(p_0,-1)$ is trapped in the closed channel $(s,0)$. The stabilization of the resonance state is reproduced in the model calculation. The critical intensities, $\alpha^{\mathrm{cir(c)}}$ and $\alpha^{\mathrm{lin(c)}}$, approximately agree with the exact values, although the maximum resonance widths are much smaller than the exact ones. The latter discrepancy is apparently ascribable to the neglect of the avoided crossings other than that considered in the two-channel model. Nevertheless, the model accurately predicts the onset of the decrease of the main energy gap, and thus the values of $\alpha^{\mathrm{cir(c)}}$ and $\alpha^{\mathrm{lin(c)}}$. The reason is because the other energy gaps to be considered have the α-dependence similar to the main energy gap.

The potential curves of the 0_{U}(cir.) and Π_{G}(lin.) manifolds in the high-frequency regime $\omega = 0.2$ are shown Fig. 15. The scenario of the stabilization for the 0_{U}(cir.) and Π_{G}(lin.) manifolds is the same as the 0_{G}(lin.) and Σ_{G}(cir.) manifolds.

The 2s state of the 0_{G}(cir.) manifold in the cases of $\omega =$ 0.2–0.6 also exhibits the stabilization as shown in Fig. 2. Since these values of ω all exceed the binding energy of the original 2s state, 0.125 a.u., these cases belong to the high-frequency regime. In the corresponding potential diagram for $\omega = 0.2$ (Fig. 7), a diabatic trapping potential can be seen when $\alpha =$ 8.0. The trapping potential coincides with the KH potential.

The stabilization of the dressed $2s$ state can thus be interpreted as the KH stabilization. The pole trajectory of $2s$ for the cases of $\omega = 0.3$, 0.4, and 0.6 exhibits the shape typical to the KH stabilization as can be seen in the case of $1s$ for $\omega = 0.6$.

The diabatic trapping potential of the 0_{G}(cir.) manifold (Fig. 13) is found to give rise to a plural number of resonances. Since the long-range part of the KH potential is Coulombic, a Rydberg series of resonances is supposed to be formed. The pole trajectories of $2s$, $3s$-$3d_0$, and $4s$-$4d_0$ in the case of $\omega = 0.4$ and 0.6 [Figs. 2(c) and 2(d)] are the members of such a Rydberg series. In the case of $\omega = 0.4$, the ground (quasibound) state of the KH potential is found to be the LIS $1s'$(cir.) when $\alpha > 1.5$. This is a reason why this LIS is named as $1s'$(cir.). On the basis of the scenario of the KH stabilization, the behavior of the $1s$,$2s$, and $3s$-$3d_0$ states of the 0_{G}(cir.) manifold can be interpreted as follows: In the case of $\omega = 0.6$ [Fig. 2(d)], all the members belong to the high-frequency regime, and all exhibit the KH stabilization. When $\omega = 0.4$ [Fig. 2(c)], the $1s$ state belongs to the intermediate-frequency regime and its behavior is not simple. However, the dressed $2s$ and $3s$-$3d_0$ states still behave in accordance with the scenario of the high-frequency regime and exhibit the KH stabilization. In addition, the LIS $1s'$(cir.) appears and exhibits the KH stabilization as if it stands proxy for $1s$. The pole trajectories for $\omega = 0.3$ [Fig. 2(c)] can be interpreted in the same fashion. When $\omega = 0.2$, however, irregular behavior is seen [Fig. 2(a)]. The energy position of the dressed $1s'$(cir.) state locates between those of the dressed $2s$ and $3s$ states. This irregularity can be ascribed to the collision between the pole trajectories of the dressed $2s$ and $1s'$(cir.) states.

As regards the case of linear polarization of $\omega = 0.2$, any diabatic trapping potential cannot be seen in the potential diagram (Fig. 10). Although some of the pole trajectories of the original excited states exhibit the stabilization [Fig. 3(a)], the mechanism cannot be explained by the trapping to the KH potential.

VI. DISCUSSION

A. Stabilization of the low-lying states

From the behavior of the dressed $2s$ state of the 0_{G}(cir.) manifold in Figs. 2(a), 2(b), 2(c), and 2(d), one can derive following rules concerning the KH stabilization: (1) The critical radius, $\alpha^{\mathrm{cir(c)}}$, decreases with increasing ω and (2) the maximum ionization rate, $\Gamma_{\max}$, decreases with increasing ω. These two rules can also be recognized in the cases of other excited states, e.g., the dressed $2p_{-1}$ state in Figs. 2(c) and 2(d). For the Σ_{G}(lin.) manifold, the behavior of the dressed $2s$ state in Figs. 3(c) and 3(d) is consistent with the above two rules. More two rules can be recognized when attention is focused on the behavior of the trajectories of the dressed $1s$ and $2s$ states in Figs. 2(d) and 3(d): Rule (3) $\alpha^{\mathrm{cir(c)}}$ dose not depend on n, and (4) $\Gamma_{\max}$ decreases with increasing n for fixed l,m, and ω. Rules (3) and (4) have been well known in the theoretical studies of the atomic ionization based on the Floquet formalism [17]. In this section, the above rules (1), (2), (3), and (4) are analyzed on the basis of the two-channel model.

An approximate formula of the critical radius is derived as follows: As shown in Figs. 2(d) and 3(d), the critical radius is reproduced by the two-channel model, in which only $(l_m,N) = (s,0)$ and $(p_0,-1)$ are considered. The critical radius can be estimated as the value of α that maximizes the energy gap of the avoided crossing between two channels. In general, the crossing point r_c between two diabatic potential curves in the channels (N,l) and $(N-1,l+1)$ can be obtained by solving the equation

$$\begin{aligned}\frac{l(l+1)}{2r_c^2} &+ V_{N,N}^{l,l,\mu_P}(r_c;\alpha) + N\omega \\ &= \frac{(l+1)(l+2)}{2r_c^2} + V_{N-1,N-1}^{l+1,l+1,\mu_P}(r_c;\alpha) + (N-1)\omega \qquad (24)\end{aligned}$$

for circular polarization. If the case of linear polarization is considerd, $V_{N,N}^{l,l,\mu_P}(r;\alpha)$ and $V_{N-1,N-1}^{l+1,l+1,\mu_P}(r;\alpha)$ should be replaced by $\tilde{V}_0^{l,l,\Lambda_P}(r;\alpha)$ and $\tilde{V}_0^{l+1,l+1,\Lambda_P}(r;\alpha)$, respectively. As can be seen from Fig. 14, the position of the crossing point is largely governed by the difference in the centrifugal repulsion between the two channels. In order to obtain a rough estimation of r_c, the approximation $V_{N,N}^{l,l,\mu_P}(r;\alpha) \simeq V_{N-1,N-1}^{l+1,l+1,\mu_P}(r;\alpha)$ [or $\tilde{V}_0^{l,l,\Lambda_P}(r;\alpha) \simeq \tilde{V}_0^{l+1,l+1,\Lambda_P}(r;\alpha)$] is adopted. It leads to the solution, $r_c = \sqrt{(l+1)/\omega}$. On the other hand, the maximum of the off-diagonal element, which causes the avoided crossing, occurs approximately at $r = \alpha/\sqrt{2}$ for the circular polarization and at $r = \alpha$ for the linear polarization. In consequence, the energy gap of the avoided crossing reaches the maximum when $\alpha = \sqrt{2}r_c$ (or $\alpha = r_c$). The critical radius is thus given by

$$\alpha_0^{\mathrm{cir(c)}} = \sqrt{2(l+1)/\omega} \qquad (25)$$

and

$$\alpha_0^{\mathrm{lin(c)}} = \sqrt{(l+1)/\omega}. \qquad (26)$$

For the ns state of the 0_{G}(cir.) and Σ_{G}(lin.) manifolds, substitution of $l = 0$ and $\omega = 0.6$ into Eqs. (25) and (26) leads to $\alpha_0^{\mathrm{cir(c)}} = 1.83$ and $\alpha_0^{\mathrm{lin(c)}} = 1.29$, which roughly coincide with the exact values [see Figs. 2(d) and 3(d)]. The formulas [Eqs. (25) and (26)] are consistent with rule (1), i.e., the critical radius decreases with increasing ω. Rule (2) can qualitatively explained as follows: As ω increases, the crossing point shifts toward small r, and potential energy at the crossing point is lowered. As a consequence, the velocity of the electron at the crossing point increases, and the probability of the nonadiabatic transition increases according to the Landau-Zener formula. As a result, the electron tends to be bound in the diabatic (KH) potential, and the ionization rate decreases. Rules (3) and (4) can be explained similarly: The electrons of the $1s$ and $2s$ dressed states are trapped in the same potential. Hence, the critical radius of these states is the same. However, the velocity of the electron of the $2s$ state is larger than that of the $1s$ state at the crossing point. As a result, the maximum ionization rate of the $2s$ state is smaller than that of the $1s$ state. The above argument is applicable to any dressed states in the high-frequency regime. In the next subsection, the stabilization of the circular Rydberg states is discussed in more detail by using the two-channel model.

B. Stabilization of the circular Rydberg states

As shown in subsection IV C, all the bound states exhibit the stabilization phenomenon in the high-frequency regime. However, the experimental observation of the stabilization phenomenon of the 1*s* state is quite difficult for the laser technology of today, because a superintense vacuum-ultraviolet laser pulse is needed. Vos and Gavrila pointed out that for highly excited Rydberg states it should be possible to detect the stabilization phenomenon by the existing experimental means [34]. For excited states with sufficiently small binding energy, the high-frequency condition can be satisfied even by infrared lasers. Moreover, in the case of linear polarization, a circular state with $|m| = l = n - 1$ is the ground state of the manifold, and its stabilization is restricted to "quasistationary (adiabatic) stabilization" (QS) since it is free from the interference stabilization [4]. Potvliege and Smith found an empirical law to predict the critical intensity at which the stabilization phenomenon starts in the case of linear polarization [35]. The empirical law can be expressed in atomic units as

$$I_{\mathrm{sc}} = \omega^3 m(l+1-m)! \tag{27}$$

According to Ref. [35], the above formula is verified for $0.04 \leqslant \omega \leqslant 0.1$ with $m = 4$, 5, and 6, $l = m, m+1$, and $m+2$, and the principal quantum number $n = l+1, l+2$, and $l+3$. Following these theoretical studies, Druten *et al.* experimentally observed the stabilization phenomenon of Ne atom in the $5g_4$ Rydberg state [24]. Piraux and Potvliege analyzed the result and concluded that it was none other than QS [25]. However, the stabilization was observed in the condition $\alpha < a_{\mathrm{at}}$, where a_{at} is the spread of the electron wave function. This fact contradicts the conventional picture that the stabilization occurs due to the dichotomy of the KH wave function which is formed when $\alpha \geqslant a_{\mathrm{at}}$ [22,23]. The radial distribution function of the circular state has the maximum at $r = n^2$, and it leads to $a_{\mathrm{at}} = n^2 = 25$ for the $5g_4$ state.

In order to study the stabilization of the circular Rydberg state, the *S*-matrix pole trajectory originating from the $5g_4$ state is calculated for the linearly polarized laser field with $\omega = 2$ eV ($=0.0735$ a.u.). The result is shown in Fig. 16. The onset of the stabilization is found to be $\alpha = 7.3$, and the behavior of the trajectory is similar to that of the dressed 1*s* state in Fig. 2(d). The present result agrees with the previous numerical studies [25,26,35], and does not support the theory based on the dichotomy of the wave function. The result of the two-channel model in the acceleration gauge including $(l_m, N) = (g_4, 0)$ and $(h_5, -1)$ is also shown in Fig. 16. The adiabatic and diabatic potential curves of the two-channel model are shown in Fig. 17. In accord with the discussion in subsection V B, the resonance state can be interpreted as a Feshbach resonance, in which the quasibound state on the KH potential of the upper channel $(l_m, N) = (g_4, 0)$ decays into the lower channel $(h_5, -1)$. It should be noted that the potential crossing exists at the classically forbidden region.

The critical radius can be calculated by Eq. (26). By substituting $l = 4$ and $\omega = 2$ eV ($=0.0735$ a.u.) into Eq. (26),

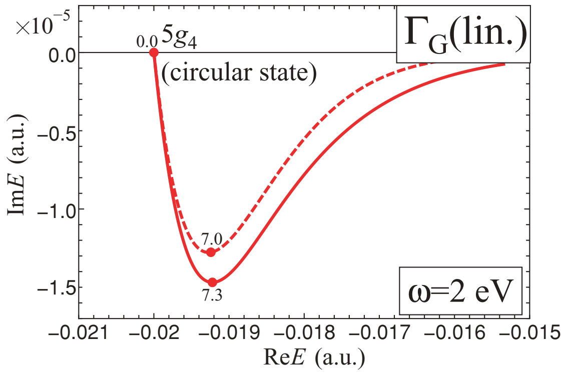

FIG. 16. (Color online) The *S*-matrix pole trajectories of the Γ_{G}(lin.) manifold in the case of $\omega = 2$ eV ($=0.0735$ a.u.). These trajectories originate from the circular state $5g_4$. The solid curve is the result obtained from the CSM with $E_{\mathrm{St}} = -0.005$. The dashed curves is the result of the two-channel model in the acceleration gauge including only $(l_m, N) = (g_4, 0)$ and $(h_5, -1)$.

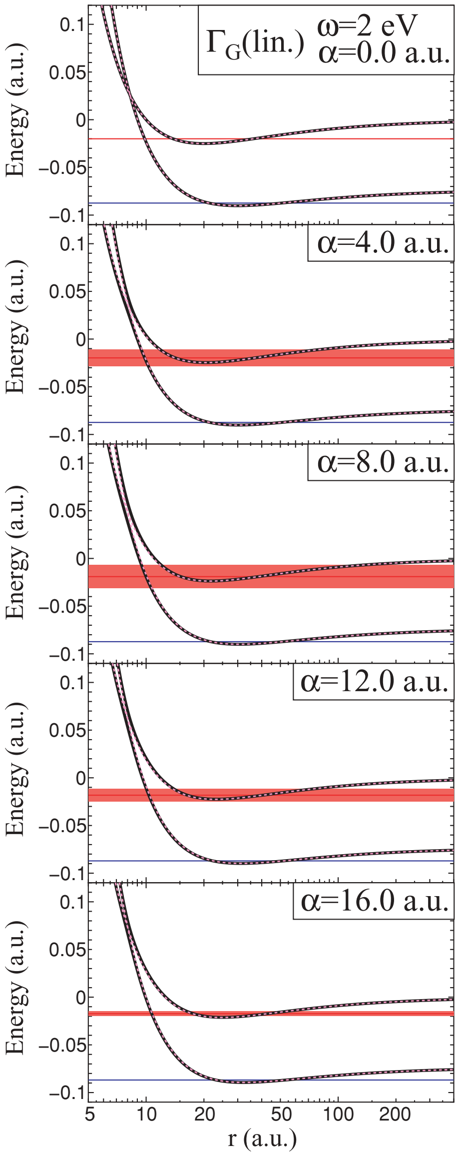

FIG. 17. (Color online) The results of the two-channel model in the acceleration gauge including $(l_m, N) = (g_4, 0)$ and $(h_5, -1)$. The meaning of the solid and dashed curves are the same as in Fig. 7. In this figure, the widths of the bands are magnified by 1000 times.

the critical radius is predicted as $\alpha_0^{\mathrm{lin(c)}} = 8.2$, which is roughly in accordance with the exact value $\alpha_0^{\mathrm{lin(c)}} = 7.3$. The critical radius is transformed to the critical laser intensity as

$$I^{\mathrm{lin(c)}} = \omega^4(\alpha^{\mathrm{lin(c)}})^2 = \omega^3(l+1). \tag{28}$$

On the other hand, the empirical law of Potvliege and Smith [Eq. (27)] is written for the circular state, $m = l$, as

$$I_{\mathrm{sc}} = \omega^3 l, \tag{29}$$

which agrees with the result of the two-channel model [Eq. (28)] for sufficiently large l. In short, the stabilization of the circular Rydberg state can be explained by the potential crossing of the two-channel model.

VII. CONCLUSION

In the present article, the ionization mechanisms of atomic hydrogen in circularly and linearly polarized laser fields are discussed within the framework of the Floquet formalism. The S-matrix pole trajectories on the complex quasienergy Riemann surface are calculated for a wide range of laser frequency based on the CSM in the velocity gauge.

In the case of circularly polarized laser field of the low-frequency regime, the pole trajectory originating from the 1s state exhibits a smooth ponderomotive energy shift implying the tunneling mechanism. In the case of linear polarization, however, the ponderomotive energy shift is interrupted by many avoided crossings among the pole trajectories. In the high-frequency regime, the pole trajectories exhibit the stabilization phenomenon. The shape of trajectory is found to be insensitive to the type of laser polarization.

These observations can be elucidated by a unified picture based on the adiabatic potentials for the radial motion of the electron in the acceleration gauge. In the case of circular polarization, the lowest adiabatic potential appears in the potential diagram of a given space-time symmetry manifold. The lowest adiabatic potential has a well and a barrier in the low-frequency regime, and the ionization can be explained by the electron tunneling through the barrier of the single adiabatic potential. The smooth ponderomotive energy shift is explicable by the gradual change in the shape of the lowest adiabatic potential. In the case of linear polarization, however, the potential curves of a given manifold possess a periodic symmetry with respect to the quasienergy. Although potential barriers can be recognized in the potential diagram for the low-frequency regime, the ionization mechanism is not explicable by a single potential curve due to nonadiabatic transitions occurring in every potential curve. This explains the reason why the ponderomotive energy shift is not smooth in the case of linear polarization. The simple picture of electron tunneling working in the case of circular polarization does not apply to the case of linear polarization. This dissimilarity originates from the difference in the space-time symmetry.

The ionization in the high-frequency regime is found to be governed by the nonadiabatic transitions at a small number of crossing points. The stabilization is explicable by the reduction of the energy gaps of the avoided crossings. In the stabilization regime, the maximum of the coupling matrix elements as a function of r move away from the crossing points with increasing laser intensity, and the energy gaps become smaller. The system behaves more diabatically, and, consequently, the electron motion is governed by the KH potential. The resonance states can be interpreted as originating from the bound states formed in the KH potential. The onset of the stabilization, i.e, the critical intensity, is shown to be predictable by the two-channel model in good approximation. The two-channel model is also useful to predict the critical intensity for highly excited circular Rydberg states, which have been attracting attention of researchers due to the possibility of experimental observation of the stabilization phenomenon [24,25]. The empirical formula of Potvliege and Smith [35] for the circular Rydebrg states is theoretically rationalized by the two-channel model in the present study.

APPENDIX A: FOURIER EXPANSION OF THE TIME-DEPENDENT POTENTIAL FUNCTIONS [EQ. (13)]

In the case of circularly polarized laser fields, the potential function in the TDSE [Eq. (9)] can be expanded in the Fourier series analytically as follows:

$$\begin{aligned}
-\frac{1}{|\boldsymbol{r}+\boldsymbol{\alpha}^{\mathrm{cir}}(t)|} &= -\sum_{l=0}^{\infty} F_l(r,\alpha/\sqrt{2})P_l\big(\cos\Theta(t)\big)\\
&= -\sum_{l=0}^{\infty}\sum_{N=-l}^{l}\frac{4\pi}{2l+1}F_l(r,\alpha/\sqrt{2})Y_{lN}^{*}\\
&\quad\times(\pi/2,-\omega t)Y_{lN}(\theta,\phi)\\
&= -\sum_{l=0}^{\infty}\sum_{N=-l}^{l} i^{N+|N|}\sqrt{\frac{4\pi}{2l+1}\frac{(l-|N|)!}{(l+|N|)!}}\\
&\quad\times F_l(r,\alpha/\sqrt{2})P_l^{|N|}(0)Y_{lN}(\theta,\phi)e^{iN\omega t}\\
&\equiv \sum_{N=-\infty}^{\infty}\sum_{l=|N|}^{\infty} C_N^l(r;\alpha)Y_{lN}(\theta,\phi)e^{iN\omega t}.
\end{aligned}\tag{A1}$$

The symbols $P_l(\cdot)$ and $P_l^{|N|}(\cdot)$ represent the Legendre polynomial and the associated Legendre polynomial, respectively, and $\Theta(t)$ is the angle between two vectors, $\boldsymbol{r}$ and $\boldsymbol{\alpha}^{\mathrm{cir}}(t)$. The function $F_l(\cdot,\cdot)$ is defined as

$$F_l(x,y) = -\frac{r_<^l}{r_>^{l+1}}, \tag{A2}$$

where $r_> = \max\{x,y\}$, $r_< = \min\{x,y\}$. In the fourth line of Eq. (A1), the Fourier coefficient $C_N^l(r;\alpha)$ is defined, which takes real value due to the appropriate choice of the phase of the laser field [Eqs. (1) and (10)].

On the other hand, in the case of linearly polarized laser fields, the Fourier transform of the potential is given by

$$\begin{aligned}
-\frac{1}{|\boldsymbol{r}+\boldsymbol{\alpha}^{\mathrm{lin}}(t)|} &= \sum_{l=0}^{\infty} F_l(r,\alpha|\cos\omega t|)P_l\big(\cos\Theta(t)\big)\\
&= \sum_{l=0}^{\infty}\sqrt{\frac{4\pi}{2l+1}}F_l(r,\alpha|\cos\omega t|)\\
&\quad\times P_l\big(\cos\theta_\alpha(t)\big)Y_{l0}(\theta,\phi),
\end{aligned}\tag{A3}$$

where $\theta_\alpha(t)$ in the second line is the angle between the vector $\boldsymbol{\alpha}_0^{\mathrm{lin}}(t)$ and z axis, and $\cos\theta_\alpha(t) = \cos\omega t/|\cos\omega t|$. The oscillation of the vector $\boldsymbol{\alpha}^{\rm lin}(t)$ makes the formula extremely complicated especially when $r < \alpha$. However, with the aid of the numerical procedure, the potential function is expanded as follows [29,31]:

$$-\frac{1}{|\boldsymbol{r}+\boldsymbol{\alpha}^{\rm lin}(t)|} \equiv \sum_{N=-\infty}^{\infty}\sum_{l=0}^{\infty}\tilde{C}_N^l(r;\alpha)Y_{l0}(\theta,\phi)e^{iN\omega t}, \tag{A4}$$

where the Fourier expansion coefficient $\tilde{C}_N^l(r;\alpha)$ is defined as

$$\begin{aligned}\tilde{C}_N^l(r;\alpha) \equiv{}& \frac{1}{\pi}\sqrt{\frac{4\pi}{2l+1}}\\ &\times\int_{-1}^{1} F_l(r,\alpha|s|)P_l(s/|s|)\frac{T_N(s)}{\sqrt{1-s^2}}ds.\end{aligned} \tag{A5}$$

Here, $T_N(s)$ is the Chebyshev polynomial defined as $T_N(\cos\omega t) \equiv \cos(N\omega t)$, and the integration is carried out numerically by using the Gauss-Chebyshev quadrature [29] (see also Ref. [31] where more accurate method for carrying out the integration [Eq. (A5)] is proposed).

APPENDIX B: THE *R*-MATRIX PROPAGATION METHOD IN THE ACCELERATION GAUGE

In this appendix, the procedure of the R-matrix propagation is briefly summarized. According to the method of Light and Walker [36], the radial coordinate is divided into many sectors. The range and the width of ith sector are denoted as $[r_{i-1},r_i]$ and $h_i \equiv r_i - r_{i-1}$ $(i = 1,2,\ldots,b)$, respectively. In the ith sector, the effective potential matrix in the close-coupling equations ([Eqs. (14) and (16)]) is evaluated at $r = r_{i-1} + h_i/2$ ignoring its r dependence within the sector. The effective potential matrix $\boldsymbol{V}(r_i;\alpha) = \boldsymbol{V}^{\rm cir}_{\mu_P}(r;\alpha)$ and $\boldsymbol{V}^{\rm lin}_{\Lambda_P}(r;\alpha)$ for circular and linear polarization, respectively, is diagonalized as

$$(\boldsymbol{T}^{(i)})^T\boldsymbol{V}(r_{i-1}+h_i/2;\alpha)\boldsymbol{T}^{(i)} = \boldsymbol{\Lambda}^{(i)}, \tag{B1}$$

and wave vector $\boldsymbol{\kappa}^{(i)}$ is defined as

$$(\boldsymbol{\kappa}^{(i)})_n = \sqrt{2[E-(\boldsymbol{\Lambda}^{(i)})_{nn}]}. \tag{B2}$$

The procedure of the R-matrix propagation in the present study is almost the same as in Ref. [36]. In order to treat complex energy, however, the sector R matrices, $\boldsymbol{r}_j^{(i)}$ $(j = 1,2,3,4)$, defined by Eq. (10) in Ref. [36] are modified as follows:

$$\left(\boldsymbol{r}_1^{(i)}\right)_{nm} = \left(\boldsymbol{r}_4^{(i)}\right)_{nm} = -\frac{1}{\kappa_n^{(i)}}\cot\left(\kappa_n^{(i)}h_i\right)\delta_{nm}, \tag{B3}$$

$$\left(\boldsymbol{r}_2^{(i)}\right)_{nm} = \left(\boldsymbol{r}_3^{(i)}\right)_{nm} = -\frac{1}{\kappa_n^{(i)}}\csc\left(\kappa_n^{(i)}h_i\right)\delta_{nm}. \tag{B4}$$

Here, the signs of the components of the vector $\boldsymbol{\kappa}^{(i)}$ need not be considered because they are canceled out in the calculation of $\boldsymbol{r}_j^{(i)}$. The R-matrix recursion is initiated at a point near the origin, $r = r_1 \ll 1$, and the initial R matrix is set as

$$\left(\boldsymbol{R}^{(1)}\right)_{Nl,N'l'} = \frac{r_1}{l+1}\delta_{NN'}\delta_{ll'}, \tag{B5}$$

according to the boundary condition [Eq. (19)]. On the asymptotic region, $r = r_b \gg 1$, the Siegert boundary condition [Eq. (18)] is imposed. The R matrix is required to satisfy the equation

$$\boldsymbol{H}^{(+)}(\boldsymbol{k}r_b,\boldsymbol{\eta})\boldsymbol{C} = \boldsymbol{R}^{(b)}\left(\frac{d}{dr}\boldsymbol{H}^{(+)}(\boldsymbol{k}r,\boldsymbol{\eta})\right)_{r=r_b}\boldsymbol{C}, \tag{B6}$$

where $\boldsymbol{C}$ is a certain unknown column vector and $\boldsymbol{H}^{(+)}(\boldsymbol{k}r,\boldsymbol{\eta})$ is the matrix representation of the Coulomb function in the form of the outgoing spherical wave. The value of the Coulomb function is calculated numerically by using the program code developed by Michel [37]. The complex quasienergies E are determined by the secular equation

$$\det\left(\boldsymbol{H}^{(+)}(\boldsymbol{\eta},\boldsymbol{k}r_b) - \boldsymbol{R}^{(b)}\left(\frac{d}{dr}\boldsymbol{H}^{(+)}(\boldsymbol{\eta},\boldsymbol{k}r)\right)_{r=r_b}\right) = 0. \tag{B7}$$

The solution is obtained by the Newton-Raphson method. Dörr *et al.* [14,15] and Noble *et al.* [16] presented similar formulation of the R-matrix propagation on the basis of the Floquet theory but in the velocity gauge.

In this article, the nonuniform sector grid is employed. The grid points are generated by the mapping function

$$r(x) = x - D\tan^{-1}\boldsymbol{(}\beta(x-x_0)\boldsymbol{)} - x_0 + \tilde{\alpha}, \tag{B8}$$

where $\tilde{\alpha} = \alpha/\sqrt{2}$ and α for circular and linear polarization, respectively, and the constant x_0 is determined by numerically solving the equation

$$\tan\left(\frac{x_0-\tilde{\alpha}}{D}\right) = \beta x_0. \tag{B9}$$

The mapping function [Eq. (B8)] is a generalization of that for the standard Coulomb problem [38]. The function [Eq. (B8)] maps the uniform grid points on the x axis to the nonuniform ones distributing more densely around $r = \tilde{\alpha}$ on the r axis. The parameters of the mapping function are set as $D = 10$ and $\beta = 0.099$.

APPENDIX C: THE CAP METHOD

The complex energy eigenvalues of the resonance in the single-channel scattering are calculated by using the complex absorbing potential (CAP) method. The numerical procedure of the CAP method is almost the same as Appendix C of Paper I, but the artificial Hamiltonian in the present study is defined as

$$H(\eta) = -\frac{1}{2}\frac{d^2}{dr^2} + V_{\rm ad}(r;\alpha) - i\eta r^6. \tag{C1}$$

The mesh points of r are chosen as $r_j = r[\Delta x(j-1/2)]$, where $\Delta x = 0.12$ and $j = 1,\ldots,400$. In the case of the $0_{\rm G}$(cir.) manifold, the numerical data of the lowest adiabatic potential $V_{\rm ad}(r;\alpha)$ at each mesh point are prepared by diagonalyzing the effective potential matrix [Eq. (22)] including the Floquet channels $N = -60,\ldots,10$. In each Floquet channel, 10 angular-momentum states are considered. The optimal value of η is determined from the minimum of $|\eta \times dE(\eta)/d\eta|$ [39,40]. The values of $\eta = 1.36 \times 10^{-8}$, 1.76×10^{-8}, 1.87×10^{-8}, 1.88×10^{-8} are used for the cases of $\alpha = 2.0, 4.0, 6.0, 8.0$, respectively. In the case of the $\Sigma_{\rm G}$(lin.) manifold, the numerical data of the lowest adiabatic potential $V_{\rm ad}(r;\alpha)$ at each mesh point are calculated by diagonalizing the effective potential matrix [Eq. (23)] constructed by the set of channels $\{(l_0,N)\,|\,l_0 = -N = 0,\ldots,60\}$ [see Fig. 1(b)]. As the optimal values, $\eta = 0.98 \times 10^{-8}$, 1.46×10^{-8}, 1.58×10^{-8}, 2.05×10^{-8} are used for the cases of $\alpha = 1.0, 2.0, 3.0, 4.0$, respectively.

---

[1] M. V. Ammosov, N. B. Delone, and V. P. Krainov, Zh. Eksp. Teor. Fiz. **91**, 2008 (1986) [Sov. Phys. JETP **64**, 1191 (1986)].

[2] M. Gavrila, J. Phys. B **35**, R147 (2002).

[3] M. Gavrila, in *Atoms in Intense Laser Fields*, edited by M. Gavrila (Academic Press, New York, 1992), p. 435.

[4] A. M. Popov, O. V. Tikhonova, and E. A. Volkova, J. Phys. B **36**, R125 (2003).

[5] H. Miyagi and K. Someda, Phys. Rev. A **80**, 023416 (2009). It is referred to as Paper I in this article.

[6] L. V. Keldysh, Zh. Eksp. Teor. Fiz. **47**, 1945 (1964) [Sov. Phys. JETP **20**, 1307 (1965)].

[7] M. Pont, N. R. Walet, M. Gavrila, and C. W. McCurdy, Phys. Rev. Lett. **61**, 939 (1988).

[8] M. Pont, Phys. Rev. A **40**, 5659 (1989).

[9] M. Pont, N. R. Walet, and M. Gavrila, Phys. Rev. A **41**, 477 (1990).

[10] M. Pont and M. Gavrila, Phys. Rev. Lett. **65**, 2362 (1990).

[11] A. Maquet, Shih-I. Chu, and W. P. Reinhardt, Phys. Rev. A **27**, 2946 (1983).

[12] R. M. Potvliege, Comput. Phys. Commun. **114**, 42 (1998).

[13] R. M. Potvliege, in *Atoms in Intense Laser Fields*, edited by M. Gavrila (Academic Press, New York, 1992), p. 373.

[14] M. Dörr, M. Terao-Dunseath, J. Purvis, C. J. Noble, P. G. Burke, and C. J. Joachain, J. Phys. B **25**, 2809 (1992).

[15] M. Dörr, P. G. Burke, C. J. Joachain, C. J. Noble, J. Purvis, and M. Terao-Dunseath, J. Phys. B **26**, L275 (1993).

[16] J. Noble, M. Dörr, and P. G. Burke, J. Phys. B **26**, 2983 (1993).

[17] M. Dörr, R. M. Potvliege, D. Proulx, and R. Shakeshaft, Phys. Rev. A **43**, 3729 (1991).

[18] R. M. Potvliege, Phys. Scr. **68**, C18 (2003).

[19] R. Shakeshaft, R. M. Potvliege, M. Dörr, and W. E. Cooke, Phys. Rev. A **42**, 1656 (1990).

[20] M. Dörr, R. M. Potvliege, and R. Shakeshaft, Phys. Rev. Lett. **64**, 2003 (1990).

[21] R. M. Potvliege and R. Shakeshaft, Phys. Rev. A **40**, 3061 (1989).

[22] J. H. Eberly, R. Grobe, C. K. Law, and Q. Su, in *Atoms in Intense Laser Fields*, edited by M. Gavrila (Academic Press, New York, 1992), p. 301.

[23] J. H. Eberly and K. C. Kulander, Science **262**, 1229 (1993).

[24] N. J. van Druten, R. C. Constantinescu, J. M. Schins, H. Nieuwenhuize, and H. G. Muller, Phys. Rev. A **55**, 622 (1997).

[25] B. Piraux and R. M. Potvliege, Phys. Rev. A **57**, 5009 (1998).

[26] O. V. Tikhonova, A. M. Popov, E. A. Volkova, and M. V. Fedorov, Phys. Rev. A **65**, 053404 (2002).

[27] *Handbook of Mathematical Functions: With Formulas, Graphs, and Mathematical Tables*, edited by M. Abramowitz and I. A. Segun (Dover, New York, 1972), Chap. 7.

[28] P. Marte and P. Zoller, Phys. Rev. A **43**, 1512 (1991).

[29] L. A. Collins and G. Csanak, Phys. Rev. A **44**, R5343 (1991).

[30] L. Dimou and F. H. M. Faisal, Phys. Rev. A **46**, 4442 (1992).

[31] L. Dimou and F. H. M. Faisal, Laser Phys. **3**, 440 (1993).

[32] L. Dimou and F. H. M. Faisal, Phys. Rev. A **49**, 4564 (1994).

[33] M. Dörr, M. Terao-Dunseath, P. G. Burke, C. J. Joachain, C. J. Noble, and J. Purvis, J. Phys. B **28**, 3545 (1995).

[34] R. J. Vos and M. Gavrila, Phys. Rev. Lett. **68**, 170 (1992).

[35] R. M. Potvliege and P. H. G. Smith, Phys. Rev. A **48**, R46 (1993).

[36] E. B. Stechel, R. B. Walker, and J. C. Light, J. Chem. Phys. **69**, 3518 (1978).

[37] N. Michel, Comput. Phys. Commun. **176**, 232 (2007).

[38] E. F. Fattal, R. Baer, and R. Kosloff, Phys. Rev. E **53**, 1217 (1996).

[39] U. V. Riss and H.-D. Meyer, J. Phys. B **26**, 4503 (1993).

[40] S. Sahoo and Y. K. Ho, J. Phys. B **33**, 2195 (2000).